Solution Property Preserving Reconstruction for Finite Volume Scheme: a BVD+MOOD framework

Siengdy Tann, Xi Deng, Yuya Shimizu, Raphaël Loubère, Feng Xiao

▶ To cite this version:

Siengdy Tann, Xi Deng, Yuya Shimizu, Raphaël Loubère, Feng Xiao. Solution Property Preserving Reconstruction for Finite Volume Scheme: a BVD+MOOD framework. International Journal for Numerical Methods in Fluids, In press, 10.1002/fld.4798 . hal-02397156

HAL Id: hal-02397156
https://hal.science/hal-02397156

Submitted on 6 Dec 2019

Solution Property Preserving Reconstruction for Finite Volume Scheme: a BVD+MOOD framework

Siengdy Tann*,[a]

Xi Deng[b], Yuya Shimizu[a], Raphaël Loubère[c,*], Feng Xiao*,[a]

[a]*Department of Mechanical Engineering, Tokyo Institute of Technology, 2-12-1 Ookayama, Meguro-ku, Tokyo, 152-8550, Japan*
[b]*Department de Mécanique, Aix-Marseille Université,58 boulevard Charles Livon, 13284 Marseille Cedex 07, Marseille, France*
[c]*Institut de Mathématiques de Bordeaux (IMB), Université de Bordeaux, 33405 Talence, France*

Abstract

The purpose of this work is to build a general framework to reconstruct the underlying fields within a Finite Volume (FV) scheme solving a hyperbolic system of PDEs (Partial Differential Equations). In an FV context, the data are piece-wise constants per computational cell and the physical fields are reconstructed taking into account neighbor cell values. These reconstructions are further used to evaluate the physical states usually used to feed a Riemann solver which computes the associated numerical fluxes. The physical field reconstructions must obey some properties linked to the system of PDEs such as the positivity, but also some numerically based ones, like an essentially non-oscillatory behaviour. Moreover, the reconstructions should be high accurate for smooth flows and robust/stable for discontinuous solutions. To ensure a Solution Property Preserving Reconstruction, we introduce a methodology to blend high/low order polynomials and hyperbolic tangent reconstructions. A Boundary Variation Diminishing (BVD) algorithm is employed to select the best reconstruction in each cell. An *a posteriori* MOOD detection procedure is employed to ensure the positivity by re-computing the rare problematic cells using a robust first-order FV scheme. We illustrate the performance of the proposed scheme via the numerical simulations for some benchmark tests which involve vacuum or near

---

*Corresponding author:

Email addresses: `tann.s.aa@m.titech.ac.jp` (Siengdy Tann), `raphael.loubere@u-bordeaux.fr` (Raphaël Loubère), `xiao.f.aa@m.titech.ac.jp` (Feng Xiao)

vacuum states, strong discontinuities and also smooth flows. The proposed scheme maintains high accuracy on smooth profile, preserves the positivity and can eliminate the oscillations in the vicinity of discontinuities while maintaining sharper discontinuity with superior solution quality compared to classical high accurate FV schemes.

Key words: Finite volume, multi-stage-BVD, THINC, positivity-preserving, MOOD,
hyperbolic system of PDEs

---

1. Introduction

Computational fluid dynamics has been widely used in many engineering and scientific research fields for decades. For instance, the conservative finite volume framework, one of the classical CFD methods is often used to solve the compressible flow problems. In recent years, high-order schemes were developed to handle both smooth and discontinuous solutions with less numerical dissipation. However, one issue of the original high-order schemes [SO88, SO89, JS96, RLZ03, ABC16] is that they may generate non-physical negative density or pressure (positivity failure), which leads to a blow-up of the numerical computation. Some classical high-order schemes fail to preserve the positivity (or to maintain the physical validity of the solution) because of interpolation errors in the vicinity of very strong discontinuities or when vacuum or near vacuum states occur. On the other hand, the first-order finite volume so-called Godunov scheme [God59, Tor09] has an excessive numerical dissipation and tends to smear out flow structures. Nonetheless, the Godunov scheme is monotone, robust and preserves the positivity. Recently, Zhang and Shu developed some positivity-preserving strategy to be supplemented with discontinuous Galerkin (DG) [ZS10, ZS11b], finite volume/difference WENO scheme [ZS11a]/[ZS12] by employing a flux limiter with a restriction on the CFL number. Other approaches based on Flux Corrected Transport (FCT) [LK16], cut-off limiters, bound-preserving strategy [XZ17] or alternative techniques are also available.

Following a different path, the Multi-dimensional Optimal Order Detection (MOOD) approach is an *a posteriori* limiting scheme which was proposed in [CDL11, DCL12, DZLD14], and further used for different families of schemes: DG context [DL16, Vil18], Lagrangian and Arbitrary-Lagrangian-Eulerian schemes [BLD15, BDLM18], or for other physical contexts apart from pure Euler equations, such as Shallow-water equation [CF17], compressible turbulence models [JYY18], hyperbolic systems with stiff source terms [BT17], Navier-Stokes equations [TB19], etc.

The main idea in a MOOD-like algorithm consists in computing a candidate numerical solution at the next time level. The MOOD algorithm picks out the bad cells from the good ones, and re-compute the bad ones using a more dissipative scheme. A cell for which the criterion of physical admissible detection (PAD) and numerical admissible detection (NAD) are satisfied is accepted for the next time step. Otherwise, if a cell does not satisfy the criteria, it is marked as problematic and re-computed by 'decrementing' the degree of the local reconstruction polynomials, expecting that a lower order scheme will deposit more dissipation in the troubled cells. This process of decrementing the local polynomial degree continues up to the cell becomes valid, or, when the lowest order possible reconstruction is attained (piece-wise constant is usually the last possibility).

Using polynomial reconstructions in an FV context is the ultra classical path followed by the majority of researchers to reach high accurate FV schemes. However, when discontinuous or step-like solutions are encountered, such polynomial reconstructions become inefficient, or, worse, counterproductive. For several years, in order to capture such discontinuous solutions, some researchers rely on the Tangent of Hyperbola INterface Capturing (THINC) method which mimics a step-like function, see for instance [XIC11, XHK05, SX14]. Later on THINC has been used in a so-called Boundary Variation Diminishing (BVD) algorithm proposed in [SIX16]. The purpose is to hybridize a WENO polynomial reconstruction with THINC functions. The BVD principle consists in appropriately selecting between these reconstructions. The diagnostics used by the BVD algorithm to select the appropriate reconstructions rely on minimizing the jump between the reconstructed values at the cell boundary. The BVD schemes are then capable to resolve both discontinuous and smooth solutions with high fidelity, see for instance [SIX16, DXL$^+$18, DIX$^+$18]. In more recent works [DSX19, DSX18], new BVD schemes have been proposed by combining high-order linear-weight (constant-coefficient) polynomials and THINC function with multi-stage BVD algorithms. The resulting schemes, so-called $\mathrm{P_nT_m}$-BVD (polynomial of n-degree and THINC function of m-level reconstruction based on BVD algorithm) schemes, are completely different from any existing high-resolution scheme that counts on nonlinear-weights polynomials to suppress spurious oscillations. Numerical verification shows that the $\mathrm{P_nT_m}$-BVD schemes are able to achieve very high order accuracy for smooth solution, and effectively remove numerical oscillation in presence of discontinuity. As shown in [DSX18], for example, a 11th order scheme can be devised by using the 10th order polynomial as one of the candidate for reconstruction.

In this paper, we present a general formulation of reconstruction in finite volume method by integrating the BVD and MOOD methodologies. As a concrete example, we propose a high-resolution scheme under a three-stage cascade BVD algorithm and MOOD method to fulfill the shock capturing and positivity-preserving properties. For BVD reconstruction algorithm, the linear 5th order upwind or piece-wise quartic method based on 4th-degree of polynomial (P4) is implemented as one of the candidate reconstruction functions to capture smooth solutions. Other candidate reconstruction functions use THINC function to eliminate the numerical oscillation and to capture sharply all discontinuities. Furthermore, a MOOD algorithm performs and detects a candidate solution by physical admissible detection (PAD) ensuring as such the positivity-preserving property. In this work, we demonstrate the effectiveness of P4-THINC-BVD-MOOD scheme, or $\mathrm{P_4T_3}$-BVD-MOOD scheme, in resolving smooth solution, capturing sharp discontinuous solution and preserving positivity via some benchmark tests.

This paper is organized as follows. In Section 2, we briefly present the general finite volume method. We demonstrate in Section 3 the details of solution property preserving reconstruction ensuring high-order accuracy (HO), essentially non-oscillation (ENO) behaviour, sharp capture of discontinuities and robustness for extreme situations. We extend the numerical scheme into two-dimensional finite volume method with a discussion on accuracy and efficiency in Section 4. In Section 5, we show the results on some benchmark tests, which testify that the present scheme is able to capture both smooth and discontinuous solutions and is able to preserve their physical validity. We end the paper with a brief summary and future plans are drawn in Section 6.

2. General Framework

For the sake of simplicity, we introduce the numerical method thoroughly in $d = 1$ dimension. Its extension to multi-dimensions, here $d = 2$, carried on by dimension splitting, is presented in a next section. Let us describe the finite volume method, the reconstruction schemes and the positivity-preserving process in the following sections.

2.1. Finite Volume semi-discretization

Let us consider a scalar hyperbolic conservation law under the form

$$\frac{\partial U}{\partial t} + \frac{\partial F(U)}{\partial x} = 0, \tag{1}$$

where $U(x,t)$ is the solution variable and $F(U)$ is the flux function. Because (1) is hyperbolic, the characteristic speed $\alpha = F'(U)$ is a real number in 1D.

The computational domain in space is defined as $\Omega = [x^L, x^R]$ and divided into N cells, $I_i = [x_{i-1/2}, x_{i+1/2}]$, for $i = 1, 2, ..., N$. The grid size is uniform over the computational domain and denoted by $\Delta x = x_{i+1/2} - x_{i-1/2}$. The time coordinate is t and $0 \leq t \leq T$, where $T > 0$ is the final time. The time interval $[0, T]$ is split into N_t time steps $[t^n, t^{n+1}]$, the time-step is non-uniform and denoted by $\Delta t = t^{n+1} - t^n > 0$, with $t^0 = 0$ and $t^{N_t} = T$.

For the standard finite volume semi-discretization, we employ the approximated volume integrated-average (VIA) of the solution $U(x,t)$ over a mesh cell I_i at time t as

$$U_i(t) = \frac{1}{\Delta x} \int\limits_{x_{i-1/2}}^{x_{i+1/2}} U(x,t)\, dx \qquad \text{where} \qquad i = 1, 2, \ldots, N. \tag{2}$$

Let us denote by $\mathsf{U} = (U_i)_{i=1,2,\ldots,N}$ the vector of discrete FV data in the mesh.

The VIA $U_i(t)$ for each cell I_i is updated by

$$\frac{dU_i}{dt} = -\frac{1}{\Delta x} \left(\widetilde{F}_{i+1/2}(t) - \widetilde{F}_{i-1/2}(t) \right), \tag{3}$$

where $\widetilde{F}_{i+1/2}(t)$ and $\widetilde{F}_{i-1/2}(t)$ are the numerical fluxes at cell boundaries, calculated by a Riemann Solver

$$\widetilde{F}_{i+1/2}(t) = F^{\text{Riemann}}_{i+1/2}(U^L_{i+1/2}, U^R_{i+1/2}, t). \tag{4}$$

where $U^L_{i+1/2}$ and $U^R_{i+1/2}$ are the left-side and right-side values at cell boundaries respectively, given by reconstructions over left and right support stencils. Particularly, the Riemann flux can be written into a canonical form as

$$F^{\text{Riemann}}_{i+1/2}(U^L_{i+1/2}, U^R_{i+1/2}, t) = \underbrace{\frac{1}{2}\left(F(U^L_{i+1/2}) + F(U^R_{i+1/2})\right)}_{\text{Central flux}} - \underbrace{\frac{|a_{i+1/2}|}{2}(U^R_{i+1/2} - U^L_{i+1/2})}_{\text{Dissipation}}, \tag{5}$$

where $a_{i+1/2}$ is a characteristic speed linked to the maximal eigenvalue of the hyperbolic conservation law. In this work a classical HLLC flux is employed [Tor09] but any approximate Riemann solver could be employed.

A reconstruction procedure is used to calculate $U^L_{i+1/2}$ and $U^R_{i+1/2}$ at given time t, we denote by $\mathcal{R}_i \equiv \mathcal{R}(\mathsf{U}, S_i)$ the reconstruction operator in cell I_i which, given the discrete solution U and a stencil S_i of neighbor cells provides a function in I_i. This reconstructed function is further evaluated at boundary points $x_{i\pm 1/2}$ to get $U^L_{i+1/2} = \mathcal{R}_i(x_{i+1/2})$ and $U^R_{i-1/2} = \mathcal{R}_i(x_{i-1/2})$ at time t.

2.2. Time integration

In order to improve the temporal accuracy for (3), the full discretization is obtained by employing a fourth-order strong stability preserving Runge-Kutta (SSPRK) developed by Ruuth and Speteri [Ruu, SR02, Got05]. Defining

$$L(U) = -\frac{1}{\Delta x}\left(\widetilde{F}_{i+1/2}(t) - \widetilde{F}_{i-1/2}(t)\right) \tag{6}$$

then the time integration is given by

$$\begin{aligned}
&U^{(1)} = U^n + 0.391752226571890\Delta t L(U^n)\\
&U^{(2)} = 0.444370493651235U^n + 0.555629506348765U^{(1)} + 0.368410593050371\Delta t L(U^{(1)})\\
&U^{(3)} = 0.620101851488403U^n + 0.379898148511597U^{(2)} + 0.251891774271694\Delta t L(U^{(2)})\\
&U^{(4)} = 0.178079954393132U^n + 0.821920045606868U^{(3)} + 0.544974750228521\Delta t L(U^{(3)})\\
&U^{n+1} = 0.517231671970585U^{(2)} + 0.096059710526147U^{(3)} + 0.063692468666290\Delta t L(U^{(3)})\\
&\;+ 0.386708617503269U^{(4)} + 0.226007483236906\Delta t L(U^{(4)})
\end{aligned} \tag{7}$$

In this work we design a Solution Property Preserving Reconstruction operator by introducing a blending of high/low order polynomials and hyperbolic tangent reconstructions.

In figure 1 we sketch the principal steps of such an FV scheme, that is the Reconstruction operator, the flux computation and the Runge-Kutta iterative method. In this paper, when Euler system of partial differential equations are considered, then the reconstructions are performed on the characteristics variables called W_1, W_2, W_3 linked to the three real eigenvalues $\lambda_1 = u - c$, $\lambda_2 = u$ and $\lambda_3 = u + c$, respectively.

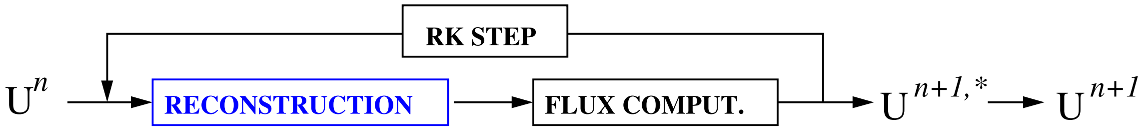

Figure 1: Sketch of the finite volume scheme with the reconstruction operator, the flux computation and the Runge-Kutta iterative method.

3. Solution Property Preserving Reconstruction

During the simulation of a hyperbolic system of partial differential equations, one generally observes large zones where the solution is regular, some discontinuities, usually of dimension $d - 1$, possibly in interaction, and, few and small but extremely demanding regions for which the correct physics is difficult to capture. These regions are the places where we have to resort numerical simulation to get an idea of the true physical solution, usually too complex to be derived as an anlytical solution. Ideally, the regular zones should be resolved with an unlimited high accurate scheme, for instance, using a piece-wise high order polynomial reconstruction. The discontinuous zones demand the use of a numerical method that can capture the discontinuity in a sharp manner and at the same time is free from spurious oscillations like a TVD 2nd order FV scheme. At last, the demanding regions of the flow can usually be dealt only with a genuinely dissipative scheme, the 1st order Godunov scheme being one of such representatives.

All of those regions are intimately related to some properties of the numerical solution which should be preserved by the numerical scheme:

- High accuracy in regular zones ⟶ Accuracy on smooth profile.

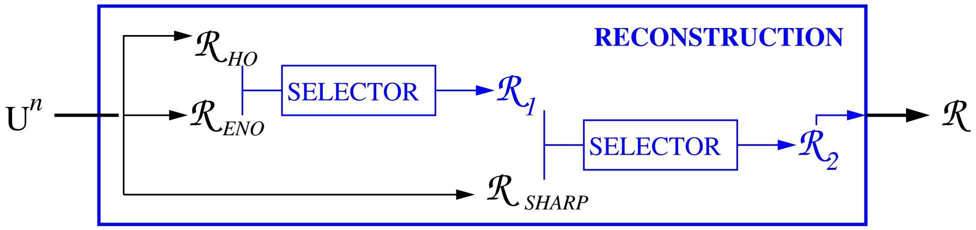

Figure 2: Illustration of the Solution Property Preserving Reconstruction. $\mathcal{R}_{\mathrm{HO}}$ is high order reconstruction operator, $\mathcal{R}_{\mathrm{ENO}}$ is an essentially non-oscillatory one, $\mathcal{R}_{\mathrm{SHARP}}$ is a sharp one. First the selector chooses between HO and ENO to get reconstruction number 1. Then the selector picks either reconstruction 1 or SHARP to get reconstruction number 2.

- Free from spurious oscillation close to steep gradient ⟶ Non oscillatory behavior.
- Sharp capture of discontinuity ⟶ Accuracy on discontinuous profile.
- Robustness for extreme situations ⟶ Fail-safe behavior

Therefore given the data U^n, the reconstruction operator should provide a reconstructed function in each cell which does generate (after the flux evaluation and the solution update) a numerical solution U^{n+1} fulfilling with the previously list of properties. We can see this problem of reconstruction as a chained cascade of different reconstruction operators. We call them $\mathcal{R}_{\mathrm{HO}}$ for high order reconstruction, $\mathcal{R}_{\mathrm{ENO}}$ for essentially non-oscillatory reconstruction, $\mathcal{R}_{\mathrm{SHARP}}$ for sharp reconstruction, see figure 2. A key tool is the so-called 'selector'. The selector chooses which reconstruction is the most appropriate one in a given cell. For instance, if the solution is smooth, the selector should select $\mathcal{R}_{\mathrm{HO}}$ reconstruction, while, in the case of a step function/shock or steep gradient, then $\mathcal{R}_{\mathrm{SHARP}}$ must be selected. Such a selector is a key point because it drives the reconstructions and, as a consequence, the numerical dissipation of the numerical method, then its accuracy. In this work the selector is acting given two candidate reconstructions in a cell, and chooses only one. Because we consider three different reconstructions, then two selectors are operating in cascade, see figure 2. Let us first present the reconstruction operators $\mathcal{R}_{\mathrm{HO}}$, $\mathcal{R}_{\mathrm{ENO}}$, $\mathcal{R}_{\mathrm{SHARP}}$. Then the selector will be described.

3.1. $\mathcal{R}_{HO}$*:* $\mathbb{P}_4$ *unlimited polynomial reconstruction*

To achieve higher accuracy in space, piece-wise polynomial reconstructions were developed within FV schemes. For instance, the piece-wise parabolic method (PPM) developed in [CW84, Huy97, LLZ15] achieves the third-order accuracy. Similarly to PPM, the fifth-order accuracy scheme based on piece-wise polynomial of degree four (P4), known as piece-wise quartic method (PQM) was proposed for instance in [WA08]. In this work we adopt the PQM reconstruction by selecting one central stencil made of five cells surrounding the current one, see figure 3, the stencil S_i is therefore constituted of cell indexes $i+k$ with $k=-2,\dots,2$. The reconstruction values at the left and right cell boundary are denoted as $U^{L,P4}_{i+1/2}$ and $U^{R,P4}_{i-1/2}$ respectively and are up-winded via the formula

$$\begin{aligned} U^{L,P4}_{i+1/2} &= \frac{1}{60}\left(2\,U_{i-2} - 13\,U_{i-1} + 47\,U_i + 27\,U_{i+1} - 3\,U_{i+2}\right) \\ U^{R,P4}_{i-1/2} &= \frac{1}{60}\left(-3\,U_{i-2} + 27\,U_{i-1} + 47\,U_i - 13\,U_{i+1} + 2\,U_{i+2}\right) \end{aligned} \tag{8}$$

This reconstruction is high accurate (5th order on smooth enough profiles in 1D) and, unfortunately, oscillatory when steep gradients are encountered.

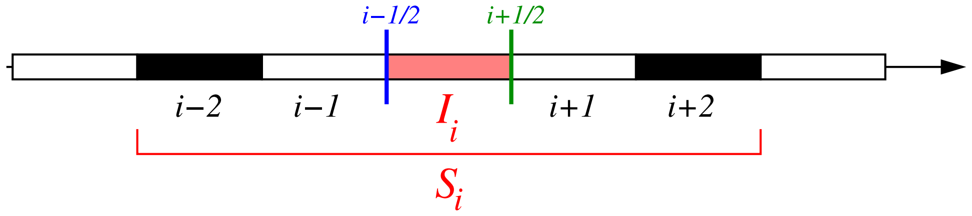

Figure 3: Stencil selection for the right/left interface $i \pm 1/2$

3.2. $\mathcal{R}_{LO}$*: no reconstruction/*$\mathbb{P}_0$ *polynomial*

When considering no reconstruction, i.e. $\mathbb{P}_0$ ‘reconstruction’, we set $U^{L,P0}_{i+1/2} = U^{R,P0}_{i-1/2} = U_i$. Such values lead to a first order FV scheme. Although it is a low accurate scheme, it presents nonetheless an extremely robust behavior. We are using this scheme as the last resort when extreme situations are encountered, such as a lack of positivity for Euler equations, occurrence of NaN, etc. see section 3.4. Obviously in this case the stencil S_i is made by only cell I_i.

3.3. $\mathcal{R}_{ENO}$, $\mathcal{R}_{SHARP}$: THINC reconstruction with $\beta \leq 1.2$ or $\beta \geq 1.6$

THINC stands for Tangent Hyperbola for INterface Capturing method, which is originally a volume of fluid (VOF) scheme employing the hyperbolic tangent function for spatial reconstruction. Being a sigmoid, differentiable and monotone function, hyperbolic tangent function mimics a step-like discontinuity. In the case of strictly increasing or decreasing set of values (U_{i-1}, U_i, U_{i+1}) then the THINC function can be expressed as [XHK05, SIX16] in I_i as

$$q_i(x) = U_{\min} + \frac{\delta U_{max}}{2}\left[1 + \theta \tanh\left(\beta\left(\frac{x - x_{i-1/2}}{x_{i+1/2} - x_{i-1/2}} - \widetilde{x}_i\right)\right)\right], \tag{9}$$

where $U_{min} = \min(U_{i-1}, U_{i+1})$, $\delta U_{max} = \max(U_{i-1}, U_{i+1}) - U_{min}$ and $\theta = \operatorname{sgn}(U_{i+1} - U_{i-1})$. The parameter β is used for controlling the slope and the jump thickness, i.e. if β has a value close to zero then the profile q_i converges towards the average value $\overline{U}_i = \frac{U_{i-1}+U_{i+1}}{2}$ while, if β is large, it tends to be a step-like function, see figure 4. In (9), the only remaining unknown, $\widetilde{x}_i$, which presents the relative location of jump center in the cell, is calculated by solving the constraint condition $U_i = \frac{1}{\Delta x}\int_{I_i} q_i(x)\, dx$. The reconstructed values at left and right ends of cell

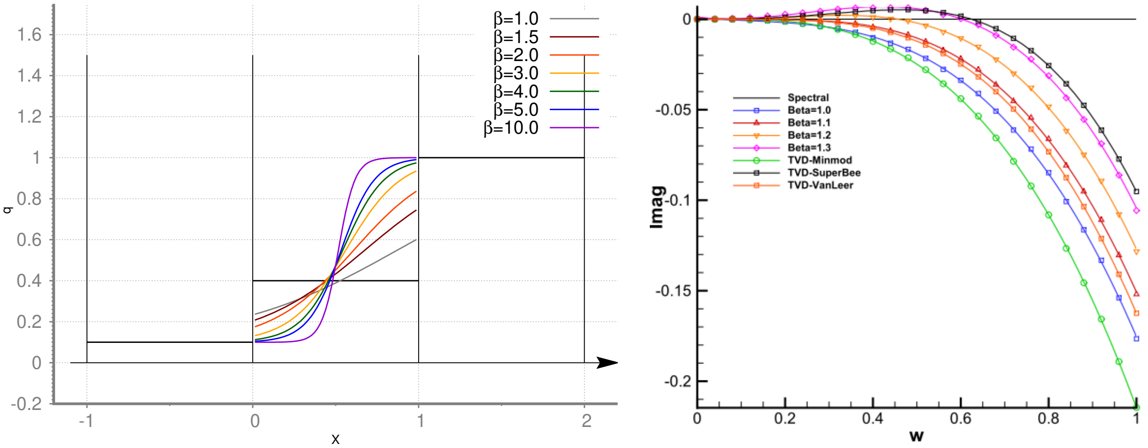

Figure 4: Left panel: Examples of THINC reconstruction $q_i(x)$ as a function of β for $\bar{q}_i = 0.4$ case over unit-length cell — Right panel: Imaginary parts of modified wave-number from THINC schemes with $\beta = 1, 1.1, 1.2$, and 1.3. The results for some TVD schemes limited with minmod, van Leer or superbee slope limiter are also displayed. (The picture focuses on small wave-numbers.)

boundary are given by

$$\begin{aligned} U_i^L(x_{i+1/2}) &= q_i(x_{i+1/2}) = U_{min} + \frac{\delta U_{max}}{2}\left(1+\theta\frac{\tanh(\beta)+A}{1+A\tanh(\beta)}\right), \\ U_i^R(x_{i-1/2}) &= q_i(x_{i-1/2}) = U_{min} + \frac{\delta U_{max}}{2}(1+\theta A), \end{aligned}$$

where $A = \frac{1}{\tanh(\beta)}\frac{B}{\cosh(\beta)-1}$, $B = e^{\theta\beta(2C-1)}$ and $C = \dfrac{U_i - U_{min}+\epsilon}{\delta U_{max}+\epsilon}$ with $\epsilon = 10^{-20}$ to avoid division by zero. We denote by $U_{i+1/2}^{L,Th\beta} = U_i^L(x_{i+1/2})$ and $U_{i-1/2}^{R,Th\beta} = U_i^R(x_{i-1/2})$ the reconstruction values for THINC's candidate interpolation function with β parameter.

Remark 1. The THINC reconstruction stencil S_i is constituted by the direct neighbors, i.e. I_{i-1} and I_{i+1}, which are only used for the computation of min and max bounds.

Remark 2.: In the case of U_i is out of the bound of $[U_{min}, U_{max}]$, which means that U_i is a local extremum and $U_i = \frac{1}{\Delta x}\int_I q_i(x)dx$ can not hold anymore, we simply set $q_i(x) = U_i$ for all point $x \in I_i$. This could be improved even further by employing a parabolic reconstruction for instance.

Remark 3.: Notice that an alternative form of (9) is

$$q_i(x) = \overline{U}_i + \frac{U_{max}-U_{min}}{2}\tanh\left(\beta\left(\frac{x-x_{i-1/2}}{x_{i+1/2}-x_{i-1/2}} - \widetilde{x}_i\right)\right),$$

from which the convergence towards $\overline{U}_i$ when β tends to 0 is evident.

$\mathcal{R}_{ENO}$: *THINC reconstruction with* $\beta \leq 1.2$. In order to avoid oscillatory behavior we employ THINC reconstructions with small values of parameter β. More precisely we use $\beta = 1.2$ or $\beta = 1.1$ which are small enough values corresponding, more or less, to the same dissipation as a 2nd order TVD FV scheme with either the van Leer slope limiter or the Minmod one respectively. The operator are respectively denoted by $\mathcal{R}^2_{\text{ENO}}$ and $\mathcal{R}^1_{\text{ENO}}$. The FV schemes associated to these operators $\mathcal{R}_{\text{ENO}}$ are therefore close to classical 2nd order TVD numerical schemes. In other words, the FV schemes generated by $\mathcal{R}_{\text{ENO}}$ reconstructions are relatively low accurate but (essentially) non-oscillatory .

In order to justify this statement, we apply the approximate dispersion relation (ADR) analysis described in [Pir06] to the THINC scheme with different wave numbers w. The numerical dissipation is quantified through the imaginary parts of the modified wave number and the results are shown on the right-panel of figure 4. Beyond $\beta \simeq 1.1$ the numerical scheme presents an anti-dissipative behavior. In order to compare with other popularly TVD schemes, we also show the numerical dissipation of the 2nd order FV scheme with Minmod, Van Leer and Superbee limiters [Lee79]. THINC scheme with $\beta = 1.1$ has a much smaller numerical dissipation than the TVD scheme employing the Minmod limiter. It presents a similar or slightly better performance than the scheme with Van Leer limiter. THINC schemes with larger parameters $\beta = 1.2$ (or 1.3) have a similar spectral property compared to the TVD method with the Superbee limiter. They both show a positive imaginary part at low wave number band leading to the well-known staircase/squaring effect [Pir06] on the solution profile. For the purpose of designing an essentially non-oscillatory scheme it is reasonable to choose THINC reconstructions with $\beta = 1.2$ and possibly $\beta = 1.1$ for a more important dissipation.

$\mathcal{R}_{SHARP}$*: THINC reconstruction with* $\beta \geq 1.6$*.* The last THINC reconstruction operator in this paper uses $\beta = 1.6$ to capture sharper discontinuous profiles by employing the staircase/squaring behavior. The associated scheme to the reconstruction operator $\mathcal{R}_{\text{SHARP}}$ is therefore anti-dissipative, leading to staircase shapes even for smooth profiles.

3.4. Robustness and physical admissibility via an a posteriori MOOD procedure

The last property corresponds to the ability of the numerical method to handle extreme physical and numerical situations, for instance the lack of positivity for density or energy for Euler equations or the occurrence of Not-A-Number (NaN) value, etc. None of the previous reconstruction procedures can ensure neither the positivity nor a fail-safe behavior. For this matter we employ the so-called *a posteriori* Multi-dimensional Optimal Order Detection (MOOD) procedure. In a MOOD algorithm a candidate solution at time t^{n+1} is tested against several goodness criteria (physical or numerical). This detection procedure separates the cells into ‘valid’ ones for which the numerical solution is accepted, and, ‘troubled’ ones. The troubled cells are locally recomputed with a first-order Godunov scheme, that is employing no reconstruction (i.e. a $\mathbb{P}_0$ polynomial). This first-order finite volume method has an excessive numerical dissipation and tends to smear out cell flow structures. However, it is known to be monotone, robust and positivity-preserving. Therefore this scheme should be used only as a last resort. The detection criteria are split into a Physical Admissible Detection (PAD) and a Numerical Admissible

Detection (NAD)

$$\text{Detect:} \qquad \text{PAD}(U_i^{n+1,*}), \qquad \text{and} \qquad \text{NAD}(U_i^{n+1,*}), \tag{10}$$

where $*$ denotes the fact that the solution is not the final one, but only a candidate solution. A cell is marked as NAD troubled if, for instance, $U_i^{n+1,*} = \texttt{NaN}$, otherwise the cell is valid. In the case of Euler equations, a cell is PAD troubled if $U_i^{n+1,*} \leq 0$ with $U = \rho$, the density or ε the specific internal energy. This corresponds to ensuring the physical admissibility of the solution for Euler equations. In the case of a linear advection equation a cell is PAD troubled if $U_i^{n+1,*} < \min_j(U_j^0)$ or $U_i^{n+1,*} > \max_j(U_j^0)$.

If the cell I_i is troubled, then it is locally recomputed by the first-order Godunov scheme. For safety reason, its direct neighbors may also be marked as troubled cells. In figure 5, we complete the sketch of a the Finite Volume scheme with an *a posteriori* MOOD procedure. Remark that only troubled cells are re-computed, which is expected to occur only in rare events. The direct neighbors of a troubled cell (i.e. sharing a flux with I_i) must also be re-updated for conservation purposes.

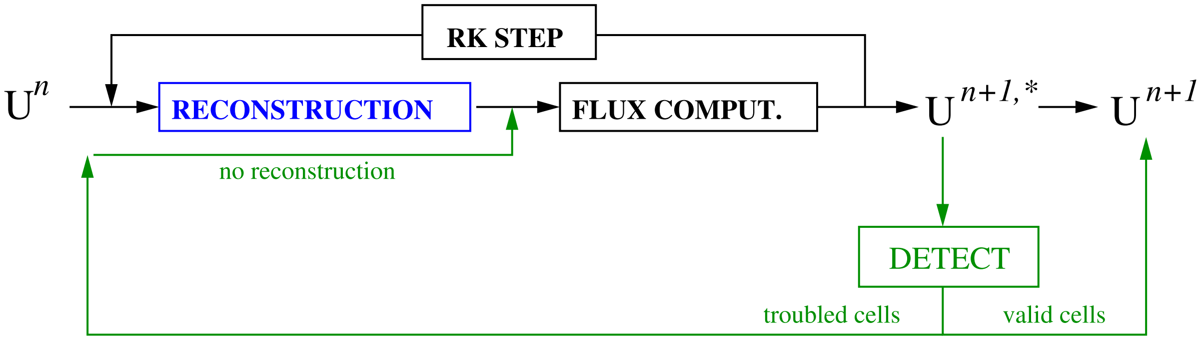

Figure 5: Sketch of the Finite Volume scheme with *a posteriori* MOOD procedure which detects troubled cells (the ones where positivity is violated, or where NaN is occurring), then recomputes the solution by a first order Godunov scheme (no reconstruction). The neighbor cells of a troubled cell must also be re-updated. Contrarily valid cells are accepted without any modification.

3.5. Illustration of the behavior of the reconstructions $\mathcal{R}$

In this section, we illustrate the behavior of the FV schemes with different reconstructions, namely using $\mathcal{R}_{\text{HO}}$ with the unlimited 5th order polynomial ($\mathbb{P}_4$), $\mathcal{R}_{\text{ENO}_2}$ with $\text{THINC}_{\beta=1.2}$,

$\mathcal{R}_{\mathrm{ENO}_1}$ with $\mathrm{THINC}_{\beta=1.1}$, $\mathcal{R}_{\mathrm{SHARP}}$ with $\mathrm{THINC}_{\beta=1.6}$ and $\mathcal{R}_{\mathrm{LO}}$ with piece-wise constant data ($\mathbb{P}_0$). Recall that the FV scheme is 1D, using a 4th order SSPRK time discretization, a HLLC flux function and one of the reconstruction operator listed above.

Smooth sine profile. Let us consider in 1D on $\Omega = [0, 1]$ the smooth function $U(x) = \sin(2\pi x)$ subject to a scalar advection equation with constant velocity $a = 1$. The domain is meshed with 20 uniform cells and 40 time iterations with $\Delta t = 0.025$ are performed. Periodic boundary conditions are considered. The exact solution consists of the same profile after one revolution. In figure 6 (left panel), we present the numerical solution obtained by each of the FV scheme using one of the 5 reconstruction operators. As expected for a smooth profile the reconstruction $\mathcal{R}_{\mathrm{HO}}$ (unlimited $\mathbb{P}_4$ FV scheme) provides the most accurate results. $\mathcal{R}_{\mathrm{ENO}_2}$ and $\mathcal{R}_{\mathrm{ENO}_1}$ produce monotone but diffuse results, with $\mathcal{R}_{\mathrm{ENO}_2}$ results being more accurate. They match approximately TVD-van Leer and TVD-superbee results. $\mathcal{R}_{\mathrm{SHARP}}$ results present the staircase behavior and $\mathcal{R}_{\mathrm{LO}}$ ones are extremely diffused.

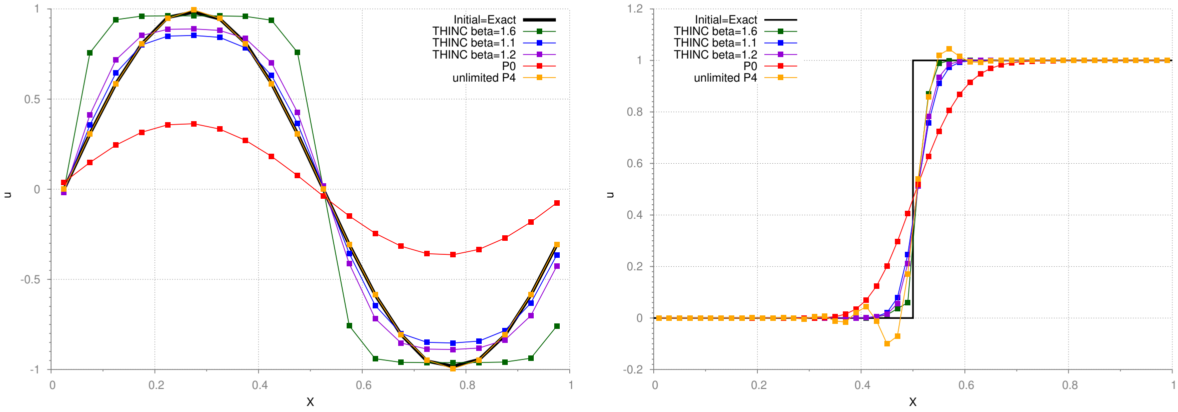

Figure 6: Advection of a sine profile (left panel) and a step profile (right panel) by the FV schemes using different reconstruction operators $\mathcal{R}$. Displays are the results of $\mathcal{R}_{\mathrm{HO}}$, $\mathcal{R}_{\mathrm{LO}}$, $\mathcal{R}_{\mathrm{ENO}_2}$, $\mathcal{R}_{\mathrm{ENO}_1}$ and $\mathcal{R}_{\mathrm{SHARP}}$ reconstructions against the exact solution.

Discontinuous step profile. Next we consider in 1D the step like function $U(x) = 1/2(1 + (x - 1/4)/|x - 1/4|)$, discontinuous at $x = 1/4$. 10 time steps and 50 uniform cells are considered. The exact solution corresponds to the initial one shifted by distance $D = 0.25$. In figure 6 (right panel), we present the results of the FV scheme with different reconstructions. As expected for a discontinuous profile, the reconstruction $\mathcal{R}_{\text{HO}}$ (unlimited $\mathbb{P}_4$ FV scheme) generates spurious oscillations but with the discontinuity maintained over $3-4$ cells. Accordingly $\mathcal{R}_{\text{LO}}$ results are monotone but truly diffusive ($\sim$ 15 cells). Contrarily the reconstructions $\mathcal{R}_{\text{ENO}_{1,2}}$ produce monotone but a somewhat diffuse discontinuity ($5-6$ cells). $\mathcal{R}_{\text{SHARP}}$ results presents a sharper discontinuity spread over the same number of cells than the one obtained with $\mathcal{R}_{\text{HO}}$ reconstruction.

The five reconstructions listed in table 1 are appropriately behaving for different situations; on regular solution, on discontinuous profile, to suppress spurious oscillations and to handle extreme situations. As a consequence it is important to correctly choose which reconstruction is the most appropriate one at a given time and location. This is the goal of the 'selector' introduced in section 3 which is designed in the following section.

Acronym	**Reconstruction**	**Parameter**	**Solution property**
HO	$\mathbb{P}_k$ unlimited polynomial	$k=4$	smooth profiles
ENO$_2$	THINC	$\beta=1.2$	(damp) spurious oscillations
ENO$_1$	THINC	$\beta=1.1$	(kill) spurious oscillations
SHARP	THINC	$\beta=1.6$	discontinuities
LO	$\mathbb{P}_0$, no reconstruction	—	positivity issue, extreme phenomena

Table 1: Table of reconstructions used in this work and their associated target property.

3.6. Local selection of reconstruction operator: a 3-stage BVD algorithm

In this work, the selector relies on a 3-stage Boundary Variation Diminishing (BVD) algorithm [SIX16, DSX19, DSX18]. The total boundary variation (TBV) in a 1D cell I_i is defined by the sum of the jumps generated by the reconstructed values (using reconstruction operator $\mathcal{R}$) at the cell interfaces:

$$\text{TBV}_i^{\mathcal{R}}(U) = \left| U_{i-1/2}^{L,\mathcal{R}} - U_{i-1/2}^{R,\mathcal{R}} \right| + \left| U_{i+1/2}^{L,\mathcal{R}} - U_{i+1/2}^{R,\mathcal{R}} \right| \geq 0. \tag{11}$$

Each term represents the amount of dissipation introduced in the numerical flux in (5) for one edge of cell I_i, therefore TBV_i scales like the numerical dissipation in the cell. When two reconstructions $\mathcal{R}_1$ and $\mathcal{R}_2$ of the same data U are available then the comparison of $\mathrm{TBV}_i^{\mathcal{R}_1}$ and $\mathrm{TBV}_i^{\mathcal{R}_2}$ allows to choose the least dissipative one in cell I_i. BVD algorithm exploits this fact. More precisely, in this work, the following 3-stage procedure is employed in spirit of [DSX19, DSX18]. Let us call the actual reconstruction used in cell i by r_i where r_i can be HO, ENO_1, ENO_2, SHARP or LO.

Stage 1. Selection between $\mathcal{R}_{\mathrm{HO}}$ and $\mathcal{R}_{\mathrm{ENO}_2} \to \mathcal{R}_{\mathrm{ST}_1}$
For all cell i, if $\mathrm{TBV}_i^{\mathcal{R}_{\mathrm{HO}}} > \mathrm{TBV}_i^{\mathcal{R}_{\mathrm{ENO}_2}}$ then $(r_{i-1}, r_i, r_{i+1}) = \mathrm{ENO}_2$, else $r_i = \mathrm{HO}$.
$\mathcal{R}_{\mathrm{ST}_1} = \{r_i,\, i = 1, \ldots, N\}$

Stage 2. Selection between $\mathcal{R}_{\mathrm{ST}_1}$ and $\mathcal{R}_{\mathrm{ENO}_1} \to \mathcal{R}_{\mathrm{ST}_2}$
For all cell i, if $\mathrm{TBV}_i^{\mathcal{R}_{\mathrm{ST}_1}} > \mathrm{TBV}_i^{\mathcal{R}_{\mathrm{ENO}_1}}$ then $(r_{i-1}, r_i, r_{i+1}) = \mathrm{ENO}_1$, else $r_i = \mathrm{ST}_1$.
$\mathcal{R}_{\mathrm{ST}_2} = \{r_i,\, i = 1, \ldots, N\}$

Stage 3. Selection between $\mathcal{R}_{\mathrm{ST}_2}$ and $\mathcal{R}_{\mathrm{SHARP}} \to \mathcal{R}_{\mathrm{ST}_3}$
For all cell i, if $\mathrm{TBV}_i^{\mathcal{R}_{\mathrm{ST}_2}} > \mathrm{TBV}_i^{\mathcal{R}_{\mathrm{SHARP}}}$ then $r_i = \mathrm{SHARP}$, else $r_i = \mathrm{ST}_2$.
$\mathcal{R}_{\mathrm{ST}_3} = \{r_i,\, i = 1, \ldots, N\}$

In the case of a scalar equation the selector (11) acts on the only variable u, while in the case of systems of three variables, say W_1, W_2, W_3 being the characteristic variables corresponding to $u - c$, u and $u + c$, respectively, we may have several options, for instance:

- W_1, W_2, W_3 may be considered as variables independent from each other, and, consequently each of them goes through the selector (11) and the selection of reconstruction. Numerical tests have shown that this option is too diffusive and the solution may even get noisy.

- W_1, W_2, W_3 are considered as variables connected each other. Extensive numerical tests have shown that an acceptable strategy then consists in
  Stage 1: the selector (11) is computed for W_1, W_2 and W_3, their neighbor cells will reconstructed based on the selection of W_3 use as $\mathcal{R}_{\mathrm{ST}_1}$
  Stage 2: the selector (11) is computed for W_1, W_2 and W_3, their neighbor cells will reconstructed based on the selection of W_1 use as $\mathcal{R}_{\mathrm{ST}_2}$
  Stage 3: each variable is independently sharpened use as $\mathcal{R}_{\mathrm{ST}_3}$.

Remark 1. In stage 1, if the THINC reconstruction is selected by W_3 for cell I_i then its two direct neighbors I_{i-1}, I_{i+1} are reconstructed with the same THINC function and also for the neighbor cells of other variables W_1 and W_2.

Remark 2. In stage 2, similar to stage 1 if the THINC reconstruction is selected by W_1 for cell I_i then its two direct neighbors I_{i-1}, I_{i+1} are reconstructed with the same THINC function and also for the neighbor cells of other variables W_2 and W_3. Indeed this cell has been selected due to a smaller TBV_i which is computed with genuinely THINC fluxes on both sides and this implies that the neighbor cells use the same reconstruction operator as I_i. The neighbor cells I_{i-1} and I_{i+1} may be mixed cells with one flux calculated by THINC reconstruction on one side and a polynomial calculated flux on the other.

The role of W_3 in stage 1 and W_1 in stage 2 could be reversed without much changes in the results. The reason why stage 3 is treated differently relies on the fact that if sharpening should be conducted (because the TBV selector says so) then it must be constructed in order to steepen any interface present for any variable. This ends the description of the 3-stage BVD algorithm.

Remark 3. The oscillation-free solution is obtained after stage 1 and stage 2 occurring. The numerical dissipation at discontinuous/steep gradients is reduced after stage 3 if needed. It means that the desired numerical solution properties are attained respectively at different stages by this multi-stage BVD approach.

Remark 4. In the multi-stage of reconstruction operators HO → ENO → SHARP → LO other TVD numerical methods could be used in replacement of THINC function with $\beta = 1.1$ or $\beta = 1.2$ (ENO). On the contrary the unlimited high order polynomial reconstruction (HO) as well as THINC with $\beta = 1.6$ used to sharpen discontinuities (SHARP) are mandatory. The first one ensures the highest possible accuracy (because no dissipative mechanism is employed), while the second one allows to maintain extremely sharp discontinuities. Up to our knowledge, we are not aware of better reconstruction operators for these situations. For the same reason, the low order (LO) scheme must be carefully chosen to ensure positivity and valid representation of numbers. In this work, the first order accurate Godunov scheme is employed as being one of the simplest and more robust positivity-preserving schemes.

Remark 5. The use of characteristics variables is not mandatory and we have experimented the BVD algorithm using the primitive variables as well. Similar to the results shown in [SIX16], using primitive variables result in somewhat more oscillatory solutions. If characteristics variables are not available, for instance when a complex tabulated equation of state is employed, then the BVD algorithm must be used with primitive variables.

4. Extension to 2D

The extension of the 2D structured grid is carried on by dimensional splitting in a straightforward manner. Our goal with this extension is to maintain the simplicity and efficiency of the method. Recall that our goal is to design a genuinely efficient and accurate limiter-free scheme, to sharply capture shocks and steep gradients, and at the same time to deal robustly with near-vacuum states. For this reason, some approximations are produced from the classical high-accurate polynomial-based FV scheme. However, it will be evident in the numerical tests, and those approximations do not deteriorate the efficiency of our non-linear numerical method. Let us directly focus on some essential points for this 2D extension.

4.1. Two dimensional finite volume framework

The computational domain is assumed to be a rectangular box $\Omega = [x^L, x^R] \times [y^L, y^R]$ divided into rectangular uniform cells $I_{i,j} = [x_{i-1/2}, x_{i+1/2}] \times [y_{j-1/2}, y_{j+1/2}]$. A point vector is denoted by a capital letter $X = (x, y)^t$. The cell center is denoted by $X_{i,j} = (x_i, y_j)^t$ and the cell sizes are Δx and Δy with $z_k = \frac{z_{k-1/2}+z_{k+1/2}}{2}$, and $\Delta z = z_{k+1/2} - z_{k-1/2}$ where z is standing for x and y, and, k for i and j respectively. We write the 2D equation of hyperbolic conservation law into

$$\frac{\partial U}{\partial t} + \frac{\partial F(U)}{\partial x} + \frac{\partial G(U)}{\partial y} = 0, \tag{12}$$

where $F(U)$ and $G(U)$ stand for the flux functions in x and y directions respectively. The numerical solution of $U(X, t)$ over a mesh cell $I_{i,j}$ at time t is approximated by a piecewise constant value

$$U_{i,j}(t) = \frac{1}{\Delta x\, \Delta y} \int\limits_{I_{i,j}} U(X, t)\, dx\, dy \qquad \text{where} \qquad i, j = 1, 2, \ldots, N. \tag{13}$$

Let us denote by $\mathsf{U}(t) = (U_{i,j}(t))_{i,j=1,2,\dots,N}$ the vector of discrete FV data in the mesh. The semi-discretization of (12) over cell $I_{i,j}$ after the application of Green theorem yields

$$\frac{dU_{i,j}(t)}{dt} + \frac{1}{\Delta x\, \Delta y} \int\limits_{\partial I_{i,j}} \mathbf{F}(U(t)) \cdot \mathbf{n}_{i,j}\, ds = 0, \tag{14}$$

where $\mathbf{n}_{i,j}$ is the outward pointing unit normal of the cell boundary $\partial I_{i,j}$, and $\mathbf{F}(U) = (F(U(t)), G(U(t)))$. Let us call the four edges forming $\partial I_{i,j}$ by $e_{i\pm 1/2,j}$ and $e_{i,j\pm 1/2}$ and rewrite the previous equation into

$$\frac{dU_{i,j}(t)}{dt} + \frac{1}{\Delta x} \left(F_{i+1/2,j}(t) - F_{i-1/2,j}(t)\right) + \frac{1}{\Delta y} \left(G_{i,j+1/2}(t) - G_{i,j-1/2}(t)\right) = 0, \tag{15}$$

which is then updated in time using the aforementioned Runge-Kutta scheme. The fluxes $F_{i\pm 1/2,j}(t)$ and $G_{i,j\pm 1/2}(t)$ are computed likewise their 1D counterparts. For instance to compute $F_{i+1/2,j}(t)$ along the vertical edge $e_{i+1/2,j}$, the left and right states, $U^L_{i+1/2,j}$ and $U^R_{i+1/2,j}$, are first computed by the use of left/right 1D reconstructions in cells $I_{i,j}$ and $I_{i+1,j}$. These reconstructions are both evaluated at the center point of edge denoted by $x_{i+1/2,j}$ at instant t for each time level as well as Runge-Kutta sub-step. Then, a Riemann solver is further employed to get the final value of the flux

$$F_{i+1/2,j}(t) = F^{\text{Riemann}}_{i+1/2,j}\left(U^L_{i+1/2,j}, U^R_{i+1/2,j}, t\right). \tag{16}$$

The same procedure is employed in y-direction to compute the fluxes $G_{i,j+1/2}(t)$. In this work a HLLC Riemann solver is used [Tor09]. Following the 1D section, a fourth-order accurate SSPRK scheme [Ruu, SR02, Got05] is employed for a high accurate time discretization.

4.2. Reconstruction operators

As previously mentioned the reconstructions are performed direction by direction. In other words, the same $\mathbb{P}_4$ reconstructions as described in (8) are first made for data aligned in x direction: $U_{i-2,j}$, $U_{i-1,j}$, $U_{i,j}$, $U_{i+1,j}$, $U_{i+2,j}$, to get the edge centered values $U^L_{i+1/2,j}$ and $U^R_{i-1/2,j}$ for cell $I_{i,j}$. Then, the 1D reconstructions in y direction consider y-aligned data $U_{i,j-2}$, $U_{i,j-1}$, $U_{i,j}$, $U_{i,j+1}$, $U_{i,j+2}$ to get values $U^L_{i,j+1/2}$ and $U^R_{i,j-1/2}$ in cell $I_{i,j}$.

The THINC reconstructions are exactly the same as in 1D, their stencils are thus restricted to two aligned neighbor cells only. The *a posteriori* MOOD loop operates also alike. The local selection of reconstruction operator follows the same algorithm depicted in section 3.6 and the

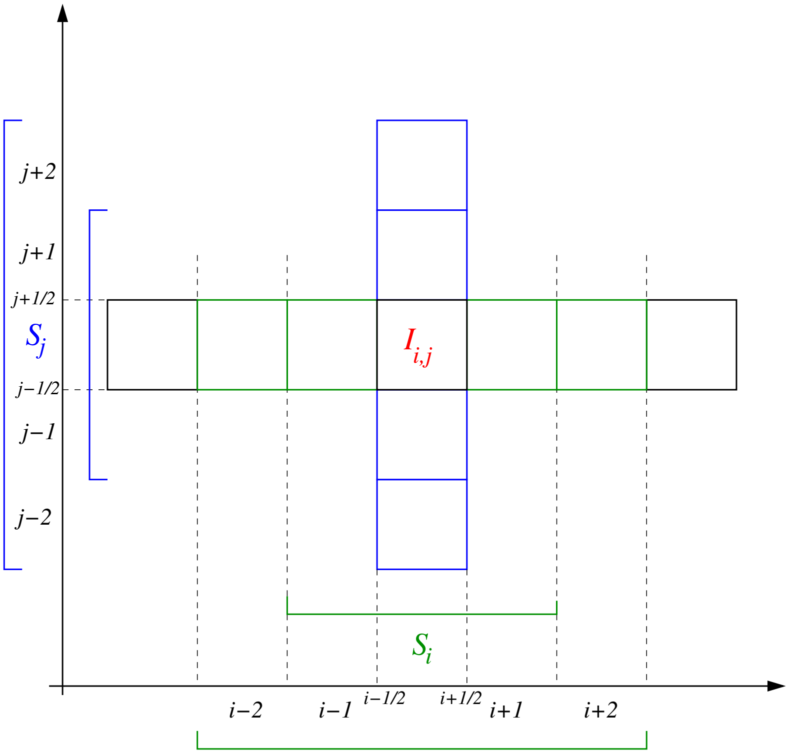

Figure 7: Stencil in 2D.

selection of reconstruction operator is independent in x and y directions.. Consequently we do not repeat those descriptions.

4.3. Discussion on accuracy and efficiency

The 1D formulation and time discretization lead to a 5th order of accuracy for smooth solution of linear advection equation as in [DSX18]. However, it is noted that our scheme is formally only second-order accurate for 1D Euler equations and in 2D due to variable dependent selection of BVD algorithm and a simple multi-dimensional implementation. Indeed the flux integration along the edges is calculated using only one integration point at the edge center. This choice has been made for three reasons. First, in order to maintain the scheme as efficient as possible, we have not multiplied the number of function evaluations ($\mathbb{P}_4$, THINC) by using Gauss quadrature points per edge, which would led to a formal 5th order accuracy for the integration, matching the target order of accuracy of the scheme. Unfortunately this would also led to a cost of 8 Riemann solvers, one for each of the 8 integration points, and, consequently, 16 function

evaluations. This is usually one of the costly part of a FV scheme. Contrarily, in our scheme, the number of function evaluations is reduced to 8 for 4 Riemann solvers.
Second, in our work the $\mathbb{P}_4$ reconstructions are not multi-dimensional ones. Hence the expected 5th order of accuracy is somewhat spoiled by the dimensional splitting during the reconstruction step. If one decides to reconstruct a true 2D $\mathbb{P}_4$ polynomial, then about 25 neighbor cell values must be used for 15 polynomial coefficients, leading to a 15×25 linear system to invert per cell.
Third, our scheme is intrinsically non-linear due to the presence of THINC reconstructions. Therefore the formal notion of 'order of accuracy on smooth flow' is more complicated to handle than for linear schemes. Only the accuracy at given mesh remains a valid and comprehensive notion, and, our 2D numerical results show that the scheme is accurate and efficient with this choice of one only integration point per edge.

Recall that the goal in this work is not to build a genuine 5th order accurate numerical method which would certainly demand true 2D polynomial reconstructions and accurate enough quadrature rule. On the contrary, this work is intended to build a genuine simple, efficient, robust and accurate enough scheme emphasizing that an appropriate mixing of linear and non-linear reconstruction operators may replace classical limiting techniques (slope/flux limiters, artificial viscosity, WENO, etc.). The following numerical section is intended to provide some numerical evidences.

5. Numerical Results

In this section, we validate the numerical scheme for some benchmark tests for a linear advection equation and the Euler equations involving strong interacting discontinuities. In addition, we also show some typical test cases involving near vacuum states to test the positivity-preserving property of the scheme. The numerical in-house FV code is built on the following key tools: the reconstruction procedure is conducted in terms of characteristic decomposition, the HLLC Riemann solver [Tor09] is used for flux computation, a SPPRK of fourth order in time discretisation is employed, the BVD algorithm for the space reconstruction is used, and, at last a *a posteriori* MOOD loop is implemented for the positivity-preservation. In order to demonstrate the performance of the present scheme, some numerical results are compared to 5th order WENO-Z scheme with the same reconstruction procedure and time discretization. The WENOZ-Z scheme generally presents good accuracy on smooth flows and a non-oscillatory behavior near discontinuity, see [FHA16, ABC16]. The numerical results produced by the current scheme in this work will be compared to this reference scheme. The CFL number is set to 0.4.

5.1. One-dimensional Linear Advection Equation

The scalar advection equation consists in considering U as a scalar field, and $F(U) = a\,U$ with a the convective velocity. We set $a = 1$ in this work. As such, any profile $U(x, t = 0)$ is convected so that the exact solution at $t \geq 0$ is given by $U(x, t) = U(x - a\,t, 0)$. For this equation the physical admissibility (PAD criteria) is set to $\min_i(U_i^0) \leq U_i^{n+1} \leq \max_i(U_i^0)$.

In order to evaluate if the present scheme can resolve different smooth profiles and discontinuity of different kinds, one simulates the test which was proposed in [JS96]. The initial condition on the computation domain $[-1, 1]$ is defined as

$$U(x,0) = \begin{cases} \dfrac{1}{6}\left(G(x,\beta,z-\delta) + G(x,\beta,z+\delta) + 4G(x,\beta,z)\right), & -0.8 \leq x \leq -0.6, \\ 1, & -0.4 \leq x \leq -0.2, \\ 1 - |10(x-0.1)|, & 0.0 \leq x \leq 0.2, \\ \dfrac{1}{6}\left(F(x,\alpha,a-\delta) + G(x,\alpha,a+\delta) + 4G(x,\alpha,z)\right) & 0.4 \leq x \leq 0.6, \\ 0, & \text{otherwise.} \end{cases} \tag{17}$$

The functions F and G are defined by

$$G(x,\beta,z)=\exp\left(-\beta(x-z)^2\right), \qquad F(x,\alpha,a)=\sqrt{\max(1-\alpha^2(x-a)^2,0)}, \tag{18}$$

and the coefficients are given by

$$a=0.5,\ z=-0.7,\ \delta=0.005,\ \alpha=10,\ \beta=\log 2/36(\delta^2). \tag{19}$$

The numerical results of the test at final time $t=2.0$ and for 200 uniform grid cells are shown in figure 8. This test is used to evaluate the occurrence of spurious numerical oscillations, the preservation of smooth and discontinuous extremes and smooth profiles. Compared to WENO-Z scheme [ABC16][1] (figure 8-(left)), the proposed scheme (figure 8-(right)) can better resolve the sharp discontinuous profiles, the step-like profile. It also effectively eliminates the numerical oscillations generated by the Gibbs phenomenon.

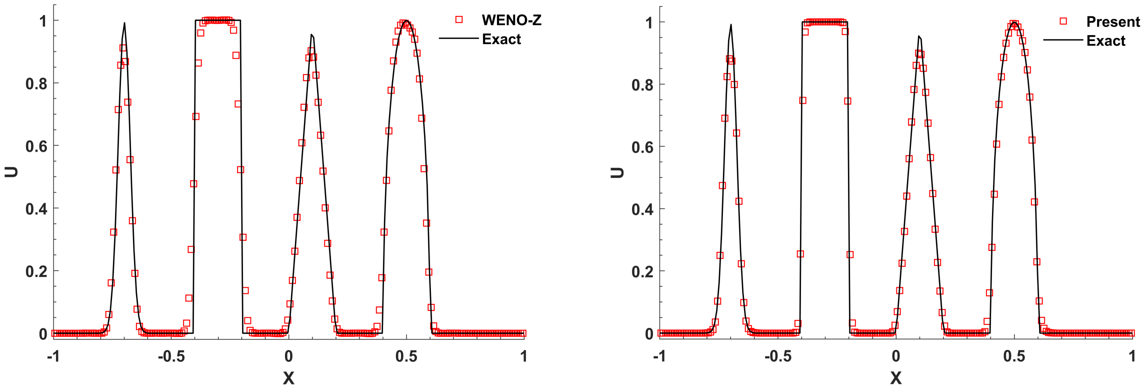

Figure 8: Numerical results for the advection of complex waves with 200 grid cells after one period ($t=2.0$) computed by WENO-Z scheme and the proposed one.

5.2. One-dimensional Euler equations

The Euler equations of compressible gas dynamics consist of conservation laws of mass, momentum and total energy with $U=(\rho,\rho u,\rho E)^T$ and $F(U)=[\rho u,\rho u^2+p,(\rho E+p)u]^T$ and

---

[1] Recall that WENO-Z has been designed in particular to avoid loss of accuracy at critical points. Hence, for this test it can be considered as a truly appropriate and adapted numerical method.

ρ, u, p are the density, velocity and pressure, respectively. E is the total energy expressed as $E = e + \dfrac{1}{2}u^2$ and e is the specific internal energy. For ideal gas, the equation of state (EOS) is defined as $p = (\gamma - 1)\rho e$ where γ is the ratio of specific heats. We set $\gamma = 1.4$ for the numerical tests if not otherwise mentioned. For the Euler equations with an ideal EOS, a candidate solution is physically admissible if $\rho_i^n > 0$ and $p_i^n > 0$ and these are the PAD criterion checked by the MOOD loop.

5.2.1. Problems involving simple waves

Double rarefaction or 123 problem. The 123 problem is one of benchmark tests presenting near vacuum state as it involves two rarefaction fans moving in opposite direction, therefore emptying a central zone. The initial condition on computational domain $\Omega = [-1, 1]$ is given in Table 2 [LR97] 400 cells are considered and the final time is set to $t_{\text{final}} = 0.6$. Outflow boundary conditions are implemented. The numerical results of the current scheme are compared to the exact solution (straight line) and represented in figure 9 with symbols. The numerical solution is in good agreement with the exact solution and the quality is comparable to positivity-preserving fifth-order finite difference WENO scheme [ZS12] and positivity-preserving DG method [ZS10]. The spurious peak in the internal energy profile is a classical flaw of many numerical methods when dealing with near vacuum state [LW03].

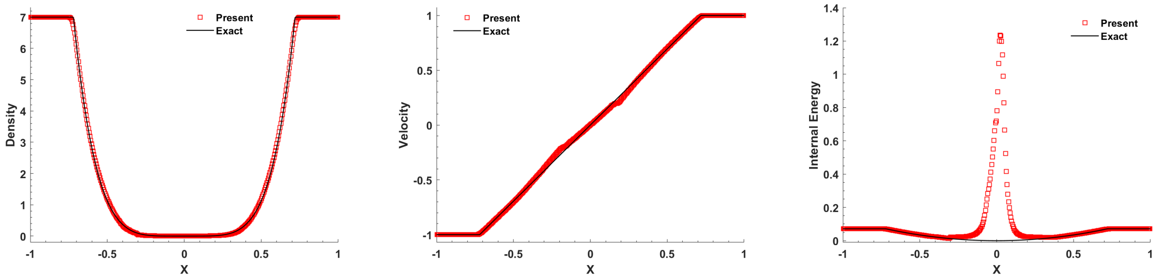

Figure 9: Numerical results for Euler equations – 123 problem – 400 cells – From left to right: density, velocity and internal energy.

Sedov blast-waves. We also evaluate the scheme on the Sedov blast-wave involving low density and low pressure [Sed59]. The initial condition is such that the density is 1, the fluid is at rest and the total energy is 10^{-12} everywhere except for the center cell where $\frac{E_0}{\Delta x}$ with $E_0 = 3.2 \times 10^6$

emulating a δ-function at the origin. The exact solution at $t > 0$ is constituted by two shock waves emanating from the origin and traveling in opposite directions and an exponentially rarefaction after the shocks leading to near-vacuum states. The computational domain is set to $\Omega = [-2, 2]$ and outflow boundary conditions are considered. The mesh size is $\Delta x = \frac{1}{200}$ and final time is $t_{\text{final}} = 0.001$. The computational results in figure 10 show that the proposed scheme provides sharp solutions for the shocks and maintains an admissible solution throughout the simulation. Notice that the original high-order reconstruction schemes like PQM [WA08] or WENO sometimes fail due to the generation of non-admissible numerical states, which leads to code termination. In this work such a situation is avoided by the *a posteriori* MOOD loop which locally uses a first-order but extremely robust scheme to cure such situations when they are observed by the detection criteria.

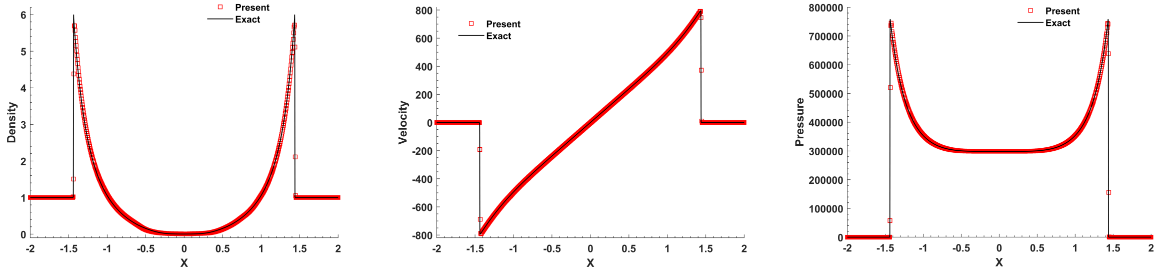

Figure 10: Numerical results for Euler equations – Sedov problem – 800 cells – From left to right: density, velocity and pressure.

Sod and Lax shock tube problems. We simulate the 1D planar Sod shock tube problem and the classical Lax shock tube problem to assess the ability of the schemes to capture simple waves. The initial conditions for density, velocity and pressure are listed in Table 2. An exact solution for both problems can be derived from the one-dimensional Riemann problem, see [Tor09]. The computational domain $\Omega = [0, 1]$ is covered by 200 cells and Dirichlet boundary conditions are imposed on both ends of the domain. The numerical solution depicted in figure 11 is is good agreement with the exact solutions. The shock waves are sharply captured essentially on one or two cells. More notably is the ability of the scheme to capture the contact discontinuity over two cells only which is a rare ability for Eulerian schemes, even for high accurate ones.

Problems	ρ_L^0	u_L^0	p_L^0	ρ_R^0	u_R^0	p_R^0	t_{final}	Ω	x_d
123	1.0	-1.0	0.2	1.0	1.0	0.2	0.6	[-2,2]	0
Sod	1.0	0.0	1.0	0.125	0.0	0.1	0.2	[0,1]	0.5
Lax	0.445	0.698	3.528	0.5	0.0	0.571	0.14	[0,1]	0.5
Le Blanc	1	0.0	$\frac{2}{3} \times 10^{-1}$	10^{-3}	0.0	$\frac{2}{3} \times 10^{-10}$	6	[0,9]	3

Table 2: Initial left and right states for the density ρ, velocity u and the pressure p for the shock tube problems. The final simulation times t_{final}, domain size and the position of the initial discontinuity x_d are also given.

Le Blanc shock tube problem. In this test, we consider the so-called Le Blanc shock tube problem with specific heat ratio $\gamma = 5/3$, with the initial condition given in Table 2. The domain is $\Omega = [0, 9]$ and the discontinuity is initially at location $x_d = 3$. This test is an extreme version of a shock tube for which the jump in density is 10^3 while the jump in pressure is 10^9 leading to violent waves, which, however are still simple waves that can be exactly computed [Tor09]. The numerical results at final time $t_{\text{final}} = 6$ are presented in figure 12 when 800 cells are used. The computed density and internal energy are plotted using a log scale to enhance the structure of the solution while we use a linear scale for the velocity. We observe that the present scheme provides a high resolution solution with sharp discontinuities without any lack of positivity. The shock wave is not at the exact location due to the fact that, for this extreme shock tube, 800 cells are not sufficient to reach the mesh convergence. Therefore, even if the numerical method is conservative and converges towards a weak solution of the Euler equations, for a coarse resolution, any numerical solution may present such misbehavior due to inaccuracy. This is classically observed for other high resolution schemes in the literature, see [LDD14, LS05, LCS09, RSS13] for a non-exhaustive variety of numerical results on this problem.

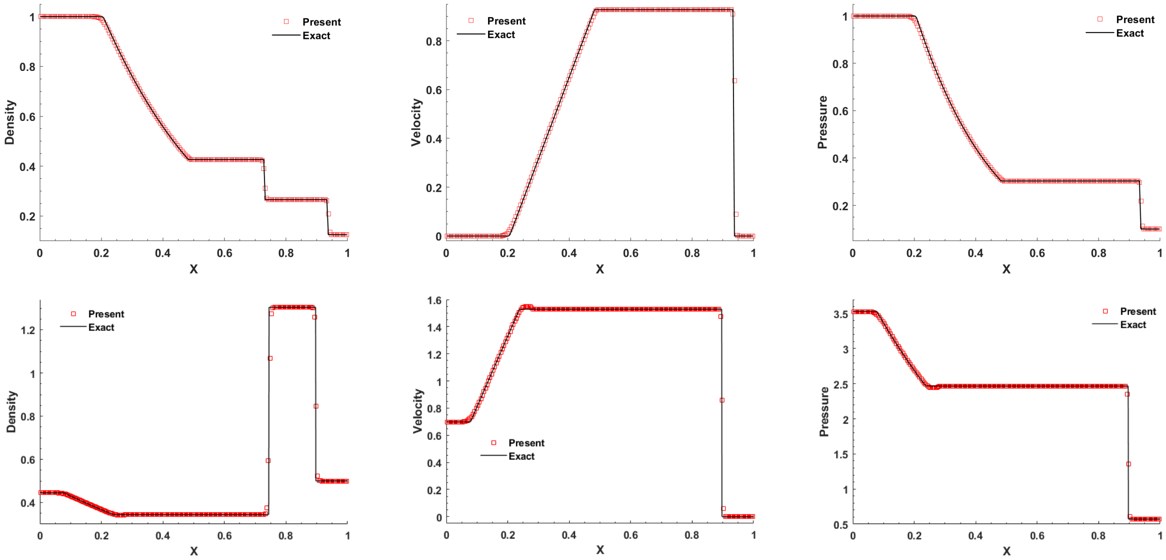

Figure 11: Numerical results for Euler equations – Sod (top) and Lax (bottom) shock tube problems – 200 cells – From left to right: density, velocity and pressure.

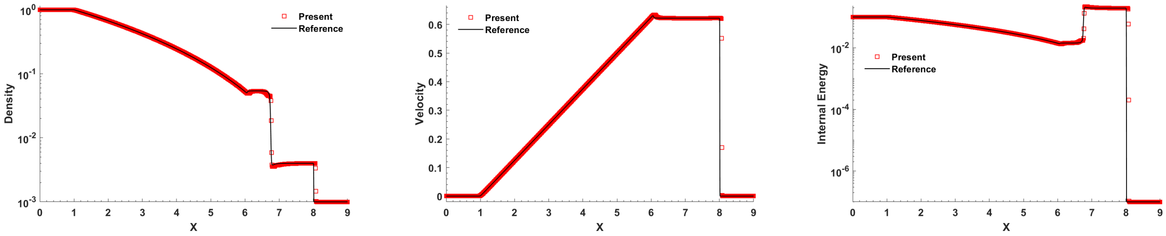

Figure 12: Numerical results for Euler equations – Le Blanc problem – 800 cells – From left to right: density, velocity and specific internal energy.

5.2.2. Problems involving interacting waves

Collela-Woodward blast-wave. This test was first introduced by Collela and Woodward [CW84] and it involves interactions of simple waves. The initial condition is given by

$$(\rho_0, u_0, p_0) = \begin{cases} (1,\ 0,\ 1000) & \text{if } 0 < x < 0.1, \\ (1,\ 0,\ 0.01) & \text{if } 0.1 < x < 0.9, \\ (1,\ 0,\ 100) & \text{otherwise} \end{cases} \tag{20}$$

and the final time is set to $t_{\text{final}} = 0.38$. Reflective boundary conditions are set on the left and right ends of the computational domain. We compute the numerical results with 400 mesh cells.

In figure 13 we observe that the proposed scheme can capture sharply the shock waves and, more notably, the contact discontinuities on very few cells (1 or 2). Recall that contrarily to classical Eulerian FV schemes based on polynomial reconstructions (with embedded limiter), our approach considers non-polynomial reconstructions (THINC) in conjunction with high accurate polynomial ones. This combination shows its importance on such test case on the left-most contact discontinuity. Obviously our approach is not exempt from drawbacks for instance the smooth region between $x = 0$ and $x = 0.5$ seems to reveal some oscillations in the velocity field. However, our numerical experiments show that using a smaller β in the first two stages effectively reduces such oscillations in velocity field.

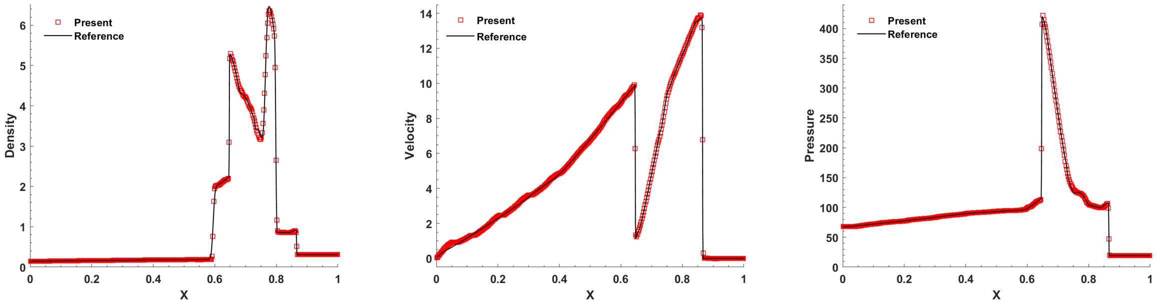

Figure 13: Numerical results for Euler equations – Collela-Woodward blast-wave problem – 400 cells – From left to right: density, velocity and pressure.

Shu-Osher oscillatory problem. This test problem [SO89, SIX16] is a particular shock tube where the downstream flow has a sinusoidal density fluctuation $\rho = 1-\varepsilon \sin(\lambda x - A)$ with a wave length of $\lambda = 50$, an amplitude of $\varepsilon = 0.2$ and the constant value $A = 25$. A Mach 3 shock front is initially located at $x = 0.1$ on domain $\Omega = [0, 1]$. The left and the right states are given by $\rho_L^0 = 3.857143$, $u_L^0 = 2.629369$, $p_L^0 = 10.33333$ and $\rho_R^0 = 1 + 0.2\sin(50x - 25)$, $u_R^0 = 0$ and $p_R^0 = 1$. The final time is $t_{\text{final}} = 0.18$. This problem involves small scale oscillating structures after the shock has interacted with the initial sine wave. We present the results for 300, 600 and 1000 uniform cells against a reference solution computed with WENO-Z scheme with 1000 cells. In figure 14 are presented the density variable (top panels) and a zoom on the oscillatory section (bottom panels) for the three mesh resolutions. We can observe that, as expected when the number of cells increases then the scheme captures more accurately the physical oscillations.

While our scheme does not outperform WENO-Z scheme on this test case, its performance is acceptable for 1000 cells. Notice that the shock wave on the left-most part of the domain presents a tiny oscillation. Also our approach can not produce accurate results for 200 cells, the selector being less performing on coarse meshes.

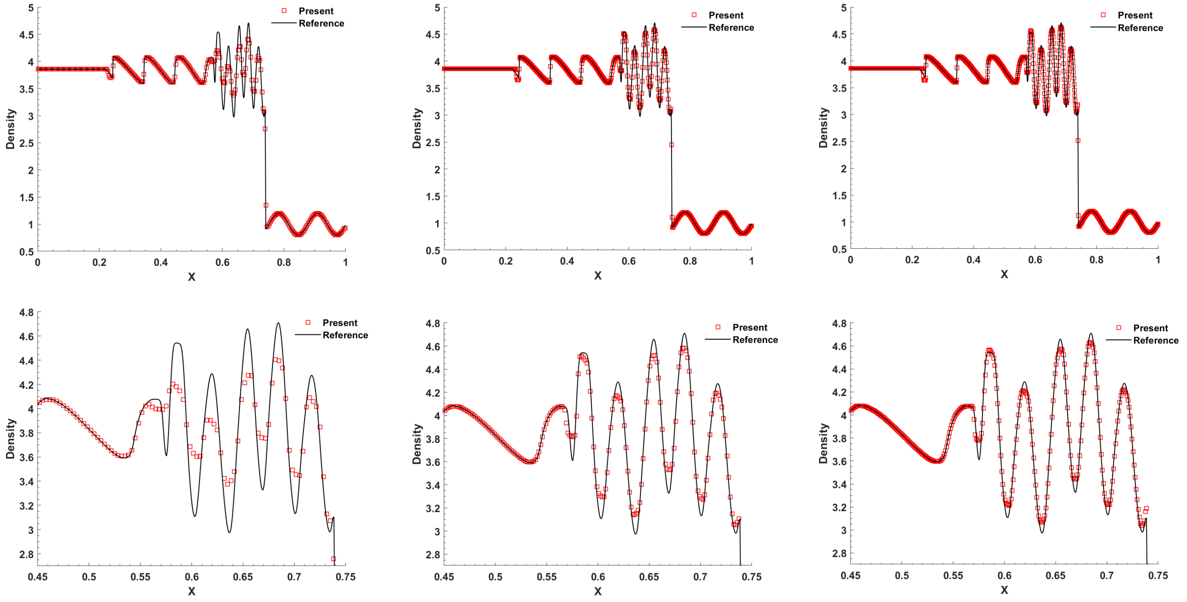

Figure 14: Numerical results for Euler equations – Shu-Osher problem – Density for 300, 600, 1000 cells from left to right – Top panels: full view – Bottom panels: zoom.

5.2.3. Diagnostics on reconstruction selection

In this section we provide some figures related to the selectors. In figure 15, for the Collela-Woodward blast-wave we color the cells according to the type of reconstruction selected (red for HO, blue for SHARP and green for ENO_1 or ENO_2) for each of the $N_t = 1605$ time-steps needed to complete the simulation in y-direction . The three characteristic variables W_1, W_2, W_3 are displayed on left, middle and right panels respectively. From this figure it is interesting to notice that the main waves and their interactions are somewhat captured. Moreover a majority of cells are dealt with the HO reconstruction (red cells), a relative important number of cells are sharpened (blue cells), and, only few need some numerical dissipation (green cells). In table 3 we present the percentage of cells dealt with the $\mathrm{HO}, \mathrm{SHARP}$, or ENO reconstructions

Test	N_t, N_c	W_1			W_2			W_3		
		SH	HO	ENO	SH	HO	ENO	SH	HO	ENO
Sod	263, 200	18.9%	43.1%	38.0%	35.8%	42.1%	22.0%	36.2%	43.8%	20.0%
Blast-w	1605, 400	15.1%	70.7%	14.3%	25.8%	64.0%	10.2%	11.0%	74.7%	14.4%
Le Blanc	1488, 800	2.2%	75.4%	22.4%	28.4%	63.4%	8.2%	8.5%	75.6%	15.8%

Table 3: Percentage of cells dealt with the SHARP, HO, ENO reconstructions for the three characteristic variables W_1, W_2, W_3 and three 1D test cases.

for Sod, Collela-Woodward and Le Blanc test cases. More precisely one sums up for all time steps the number of cells using the same reconstruction and take the percentage with respect to the total number $N_t \times N_c$. As expected the percentages in table 3 do not allow to extract a general behavior because each test case presents different flow characteristics which demand the adaptation of the scheme and its reconstructions. However it seems that the optimally accurate HO reconstruction is chosen for 40% up to 75% of cells. In other words those cells are updated with the 5th order of accuracy without any dissipation mechanism. The dissipative ENO reconstructions are chosen for 10% up to 38% of cells to avoid spurious oscillations. At last the sharp reconstruction is selected for 2% up to 36% of cells.

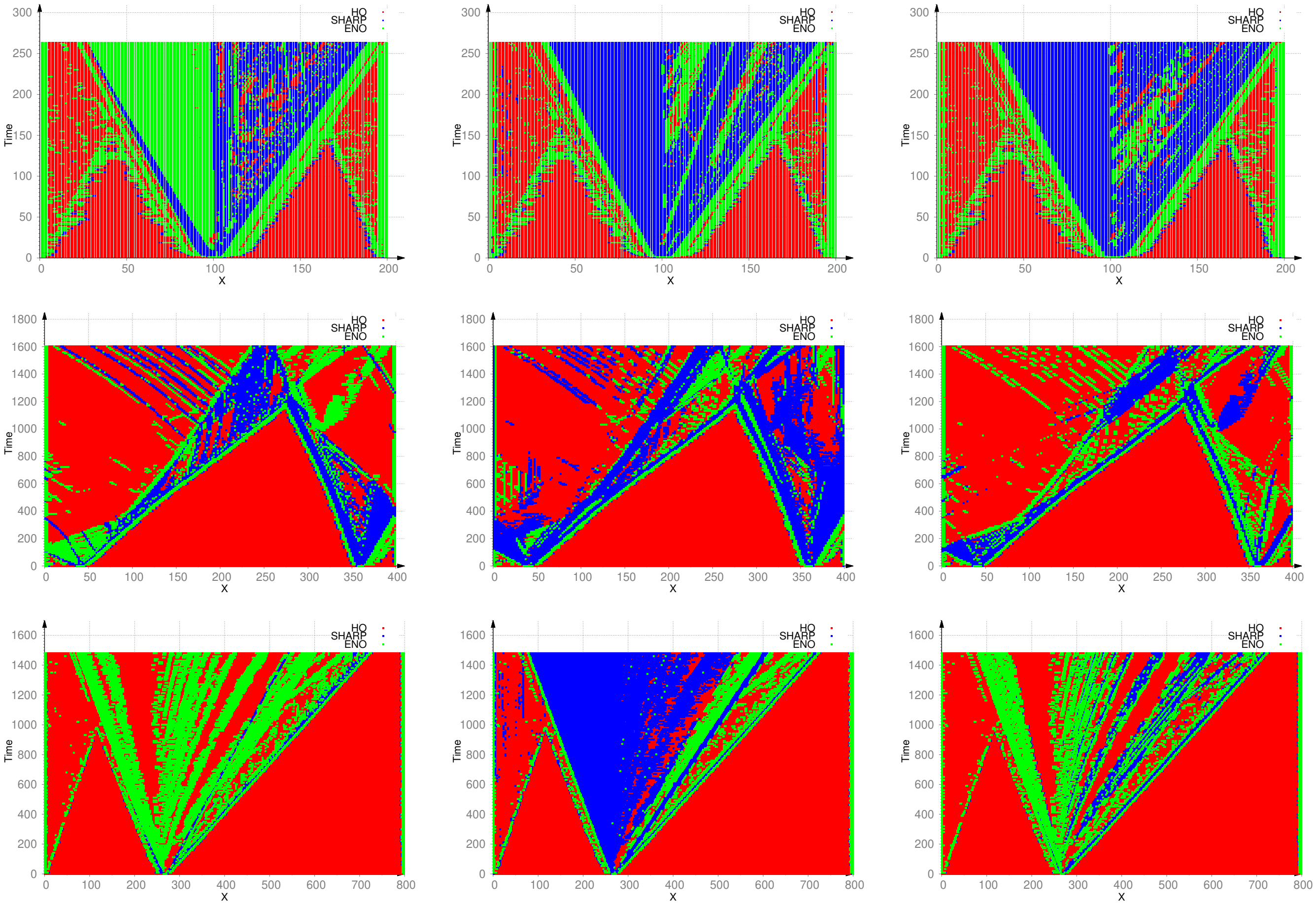

W_1 W_2 W_3

Figure 15: Numerical results for Sod (top panels), Collela-Woodward blast-wave (middle panels) and Le Blanc (bottom panels) problems – Cell number in x axis, time iteration in y axis – Each cell (x-direction) is colored according to the selector as a function of time-steps, red for HO, blue for SHARP and green for ENO_1 or ENO_2 reconstruction – From left to right: characteristic variables W_1, W_2, W_3.

5.3. Two-dimensional Euler equations

5.3.1. Riemann problems

In order to verify that the multi-stage BVD-MOOD scheme is accurate, robust, and produces non-oscillatory solutions, we test a set of two-dimensional Riemann problems which have been introduced and widely studied in [SR93, KT02]. Recently, Balsara *et al* [Bal10, Bal12, BDA14], have employed the 2D Riemann problems to build a genuinely multi-dimensional HLL type Riemann Solvers. The computational domain is $\Omega = [-0.5, 0.5] \times [-0.5, 0.5]$ and the initial conditions are given by

$$\mathbf{u}(x, y, t = 0) = \begin{cases} \mathbf{u}_1 & \text{if} \quad x > 0 \land y > 0, \\ \mathbf{u}_2 & \text{if} \quad x \leq 0 \land y > 0, \\ \mathbf{u}_3 & \text{if} \quad x \leq 0 \land y \leq 0, \\ \mathbf{u}_4 & \text{if} \quad x > 0 \land y \leq 0. \end{cases} \tag{21}$$

#		ρ	u	v	p	ρ	u	v	p	t_{final}
		$x \leq 0$				$x > 0$				
RP1	$y > 0$	0.5323	1.206	0.0	0.3	1.5	0.0	0.0	1.5	0.3
	$y \leq 0$	0.138	1.206	1.206	0.029	0.5323	0.0	1.206	0.3	
RP2	$y > 0$	0.5065	0.8939	0.0	0.35	1.1	0.0	0.0	1.1	0.25
	$y \leq 0$	1.1	0.8939	0.8939	1.1	0.5065	0.0	0.8939	0.35	
RP3	$y > 0$	2.0	0.75	0.5	1.0	1.0	0.75	-0.5	1.0	0.30
	$y \leq 0$	1.0	-0.75	0.5	1.0	3.0	-0.75	-0.5	1.0	
RP4	$y > 0$	1.0	-0.6259	0.1	1.0	0.5197	0.1	0.1	0.4	0.25
	$y \leq 0$	0.8	0.1	0.1	1.0	1.0	0.1	-0.6259	1.0	
RP5	$y > 0$	1.0	0.7276	0.0	1.0	0.5313	0.0	0.0	0.4	0.25
	$y \leq 0$	0.8	0.0	0.0	1.0	1.0	0.0	0.7276	1.0	

Table 4: Initial conditions for the 2D Riemann problems numbered from 1 to 5. These further correspond to Configurations 3, 4, 6, 8 and 12 in [KT02]

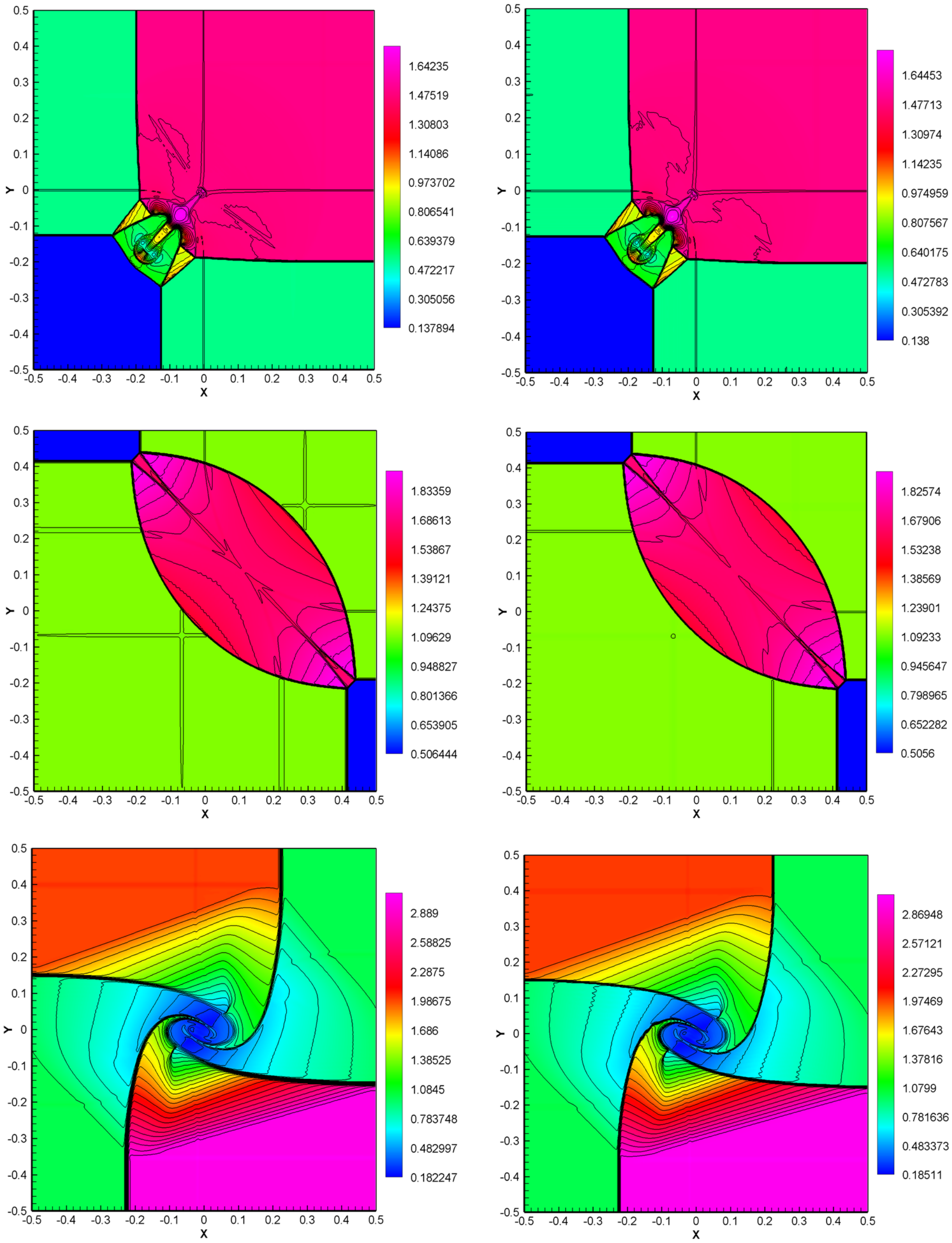

Figure 16: Numerical results for Riemann problems computed by WENO-Z and the present scheme with 400×400 mesh cells – 30 contours from min and max values for density – Left: WENO-Z scheme; Right: Present scheme.

The initial conditions and the final solution time, t_{final}, for the five configurations tested in this article are listed in Table 4. For more information about the other configurations the

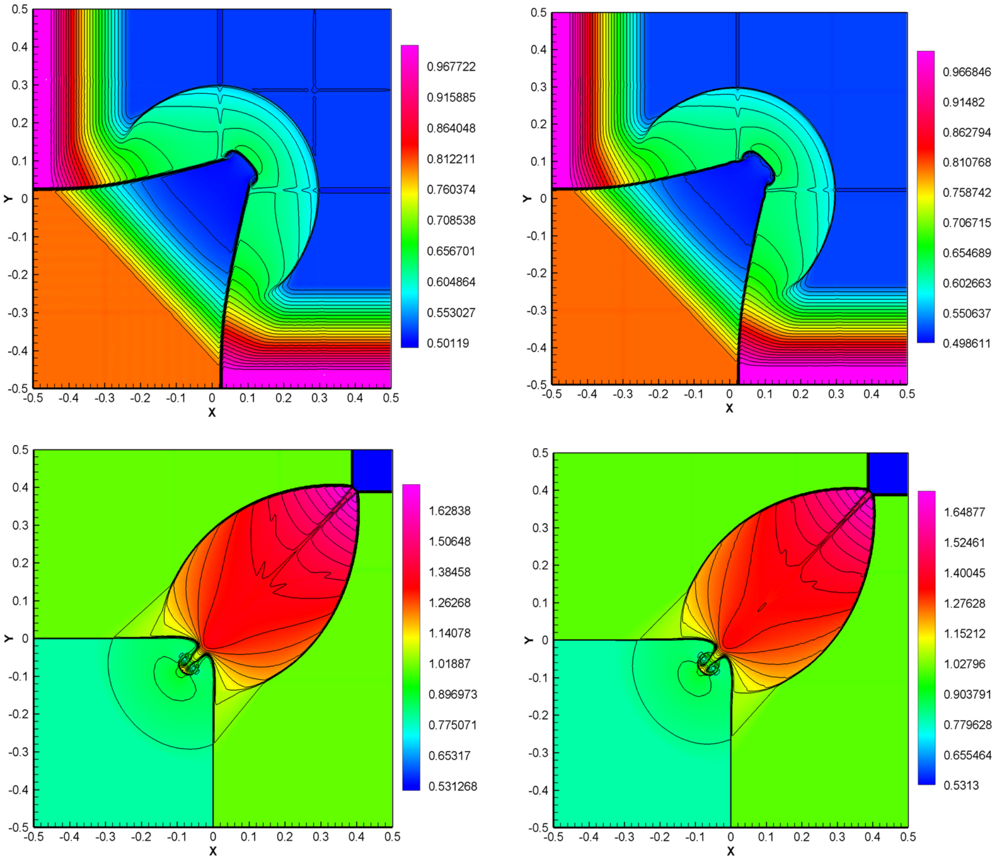

Figure 17: Numerical results for Riemann problems computed by WENO-Z and the present scheme with 400 × 400 mesh cells – 30 contours from min and max values for density – Left: WENO-Z scheme; Right: Present scheme.

reader is referred to [SR93, KT02]. For the computation we have employed a uniform grid of 400×400 mesh cells for both schemes (WENO-Z and multi-stage BVD-MOOD). The numerical solutions are illustrated for the first three and the last two configurations in figure 16 and 17, respectively. In the left panels and the right panels we respectively show the density profile at the final time computed by WENO-Z and present scheme, with 30 equidistant iso-lines between the minimum and maximum values. We observe that the computational results of two schemes equivalently produce numerical solutions for the main flow structures of all 2D Riemann problems with this mesh. Therefore, the multi-stage BVD-MOOD scheme performs well in capturing the discontinuities without spurious oscillations and also without excessive numerical dissipation for the smooth part of the flow structures. Furthermore, we also show the results of RP3 for

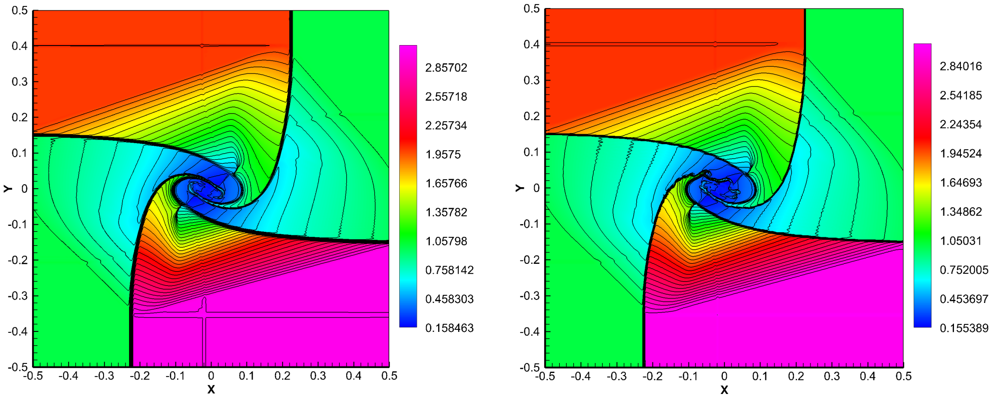

Figure 18: Numerical results for Riemann problems computed by WENO-Z and the present scheme with 600×600 mesh cells – 40 contours from min and max values for density – Left: WENO-Z scheme; Right: Present scheme, showing the Kelvin-Helmholtz instability on the shear waves.

both schemes with 600×600 mesh cells in figure 18. We can observe that the present scheme has better performance than WENO-Z scheme by showing the birth of the Kelvin-Helmholtz instability on the shear waves as an evidence of a lower dissipation.

5.3.2. Double Mach reflection

Next we have run the 2D double Mach reflection problem of a strong shock that was proposed by Woodward and Colella [WC84]. This test problem involves a Mach 10 shock in a perfect gas with $\gamma = 1.4$ which hits a 30° ramp with the x-axis. Using Rankine-Hugoniot conditions we can deduce the initial conditions ($t = 0$) in front of and after the shock wave

$$(\rho, u, v, p)(x, y, 0) = \begin{cases} (8.0, 8.25\cos(\pi/6), -8.25\sin(\pi/6), 116.5), & \text{if} \quad x < x_0 = \frac{1}{6} + \frac{y}{\sqrt{3}}, \\ (1.4, 0.0, 0.0, 1.0), & \text{if} \quad x \geq x_0 = \frac{1}{6} + \frac{y}{\sqrt{3}}, \end{cases}$$

on the domain $\Omega = [0, 3.2] \times [0, 1]$. Reflecting wall boundary conditions are prescribed on the bottom and inflow and outflow boundary conditions on the left side and the right side, respectively. The exact solution of an isolated moving oblique shock wave with Mach number $M_s = 10$ is imposed on the upper boundary. The location of shock-wave at any time t on top boundary $y = 1$ is $s(t) = x_0 + \frac{1+20t}{\sqrt{3}}$. The boundary conditions on the top boundary are therefore given by

$$(\rho, u, v, p)(x, y = 1, t) = \begin{cases} (8.0, 8.25\cos(\pi/6), -8.25\sin(\pi/6), 116.5), & \text{if} \qquad 0 \leq x < s(t), \\ (1.4, 0.0, 0.0, 1.0), & \text{if} \qquad s(t) \leq x \leq 4 \end{cases}$$

and the final time is set to $t_{\text{final}} = 0.2$. The mesh is made of $N_x \times N_y$ cells with $N_x = 320, 640, 960$ and $N_y = 100, 200, 300$, respectively. Although there exists no exact solution for this problem, it has become a classical bench-marking test in the literature because it involves shock waves and smooth recirculating flow zones. In figure 19 we present the density variable in color with 30 contour iso-lines spanning the interval $[1.4, 22.5]$ computed by three different grid resolutions, $\Delta x = \Delta y = \dfrac{1}{100}$ for the top panels, $\Delta x = \Delta y = \dfrac{1}{200}$ for the middle panels and $\Delta x = \Delta y = \dfrac{1}{300}$ for the bottom panels of figure 19. The zoomed-in part of the numerical results are presented in figure 20. The results obtained by the present scheme and those simulated by high order schemes in [FHA16] (page 352 and figure 17) are in good agreement. Moreover, the present scheme has properly detected the shock waves without spurious oscillations and the vortexes along the slip line are more visible as shown by the fine grid computation.

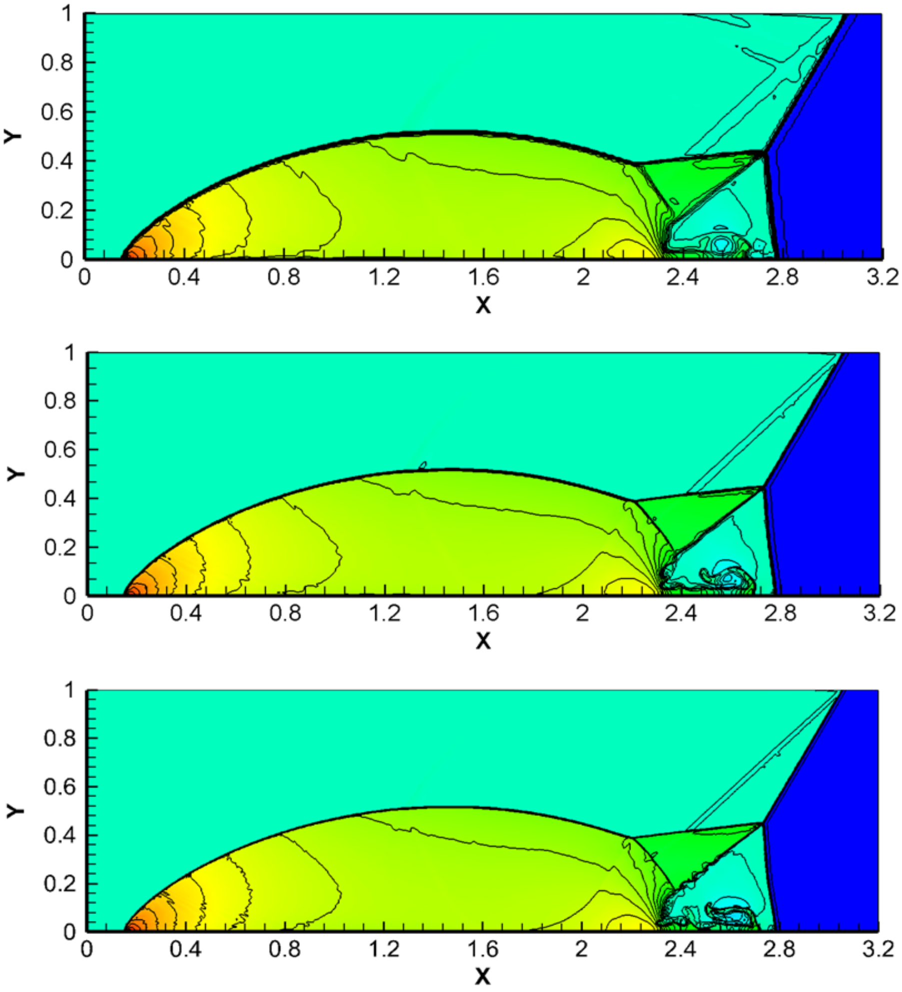

Figure 19: Numerical results for the 2D Euler equations – Double Mach reflection problem at time $t = 0.2$ simulated by the present scheme with different mesh numbers – Density variable in colour and with 30 contour iso-lines spanning the interval $[1.4, 22.5]$ – Top panels: 320×100 mesh cells; Middle panels: 640×200 mesh cells; Bottom panels: 960×300 mesh cells.

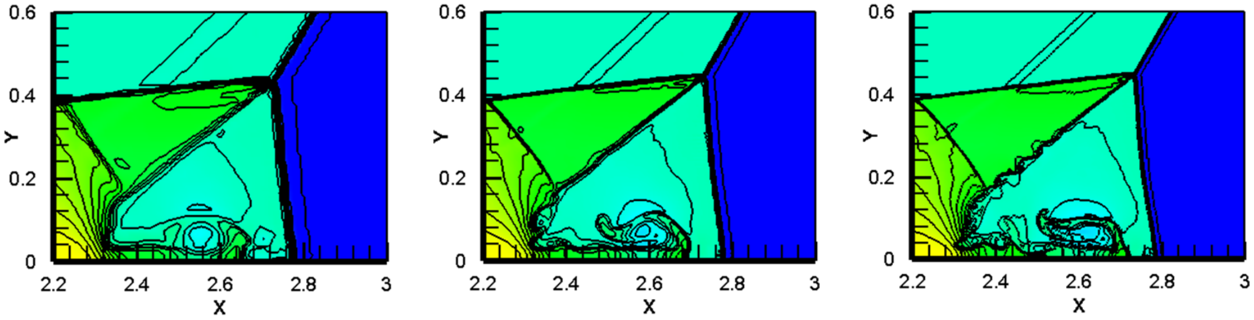

Figure 20: Zooms in the numerical solutions displayed in figure 19 – Double Mach reflection problem at time $t = 0.2$ simulated by the present scheme with different mesh numbers – Density variable in colour and with 30 contour iso-lines spanning the interval $[1.4, 22.5]$ – From left to right: 320×100 mesh cells; 640×200 mesh cells; 960×300 mesh cells.

5.3.3. Shock-vortex interaction

Another classical test in two space dimensions is the interaction of a vortex with a steady shock wave. Originally proposed by [RCD03], this test involves complex flow patterns with smooth features and discontinuous waves. The initial conditions, defined over the computational domain $\Omega = [0,1] \times [0,1]$, are given by a stationary normal shock wave placed at $x = 0.5$ and by a vortex, which is centered at $(x_c, y_c) = (0.25, 0.5)$. The left and right states separated by the shock wave are given by

$$(\rho, u, v, p)(x, y, 0) = \begin{cases} (1, \sqrt{\gamma}, 0, 1), & \text{if} \quad x < \frac{1}{2}, \\ \left(\frac{\gamma-1+1.3(\gamma+1)}{\gamma+1+1.3(\gamma-1)}, \sqrt{\gamma} - \sqrt{2} \left(\frac{0.3}{\sqrt{\gamma-1+1.3(\gamma+1)}} \right), 0, 1.3 \right), & \text{if} \quad x \geq \frac{1}{2}, \end{cases}$$

The left state is supplemented by an isentropic vortex of the form

$$(\delta u, \delta v) = \left(\varepsilon \frac{y - y_c}{r_c} e^{\alpha(1-r^2)}, -\varepsilon \frac{x - x_c}{r_c} e^{\alpha(1-r^2)} \right), \quad \delta T = -\varepsilon^2 \frac{\gamma - 1}{4\alpha\gamma} e^{2\alpha(1-r^2)},$$

with $r^2 = \dfrac{\|X - X_c\|^2}{r_c^2}$. The numerical simulations are performed over a uniformly mesh using 200 grid points per direction. Transmitive boundary conditions are imposed on the boundary and the final time is taken to be $t_{\text{final}} = 0.5$. The remaining parameters are set to $\varepsilon = 0.3$, $\alpha = 0.204$ and $r_c = 0.05$. In figure 21 we present the 30 contours of density profile spanning $[0.998296, 1.30234]$ at final time for the WENO-Z (left panel) and $[0.997274, 1.29747]$ for the present scheme (right panel). We observe that both of the schemes have captured appropriately the shock waves without spurious oscillations as well as the smooth solution region. The CPU times observed for both schemes are 1953 seconds for WENO and 6% more expensive for the present scheme (2070 seconds) both ran on DEV-C++ Integrated Development Environment. Hence, the present scheme can reproduce the quality of WENO-Z results for a comparable CPU time.

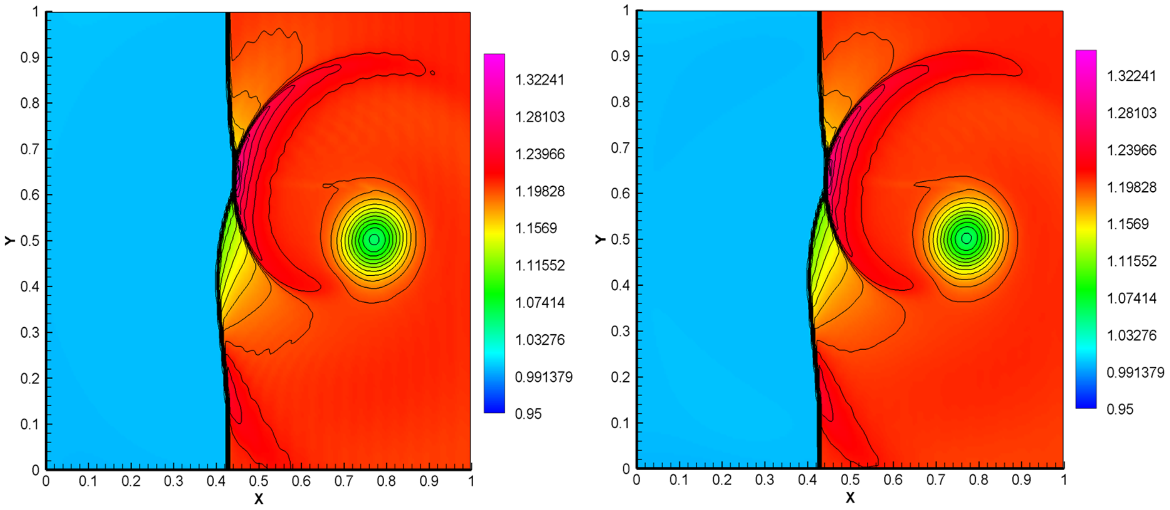

Figure 21: Numerical results for the 2D Euler equations – Shock-vortex interaction problem at final time – 30 contours from 0.95 to 1.35 for density – Left: WENO-Z scheme; Right: Present scheme.

5.3.4. The 2D Sedov Blast Waves

For this cylindrical Sedov test [Sed59], the computational domain is reduced to $[0, 1.2] \times [0, 1.2]$ where only the lower left corner cell contains the high energy of a perfect gas at rest ($\gamma = 1.4$). The initial condition is given by

$$(\rho_0, u_0, v_0, p_0) = \begin{cases} (1,\ 0,\ 0,\ \dfrac{0.244816}{\Delta x \Delta y}) & \text{if } x < \Delta x \quad \text{and} \quad y < \Delta y \\ (1,\ 0,\ 0,\ 4 \times 10^{-13}) & \text{otherwise,} \end{cases} \tag{22}$$

where $\Delta x = \Delta y = \dfrac{1.2}{120}$ (120×120 square cells) and the final time is $t_{\text{final}} = 1$. For the boundary conditions, an outflow boundary is applied to the right and upper boundaries while a reflective boundary is considered on the left and bottom boundaries. Figure 22 shows the density profiles computed by the present scheme at final time. We can observe that the results are in good agreement with the exact solution as a function of cell radius on the first panel. The cylindrical waves (shock and rarefaction) is well captured and preserved and the shock is maintained on few cells. Even though the value of density is very low towards the origin, the present scheme can simulate the test without any blow-up or code crash.

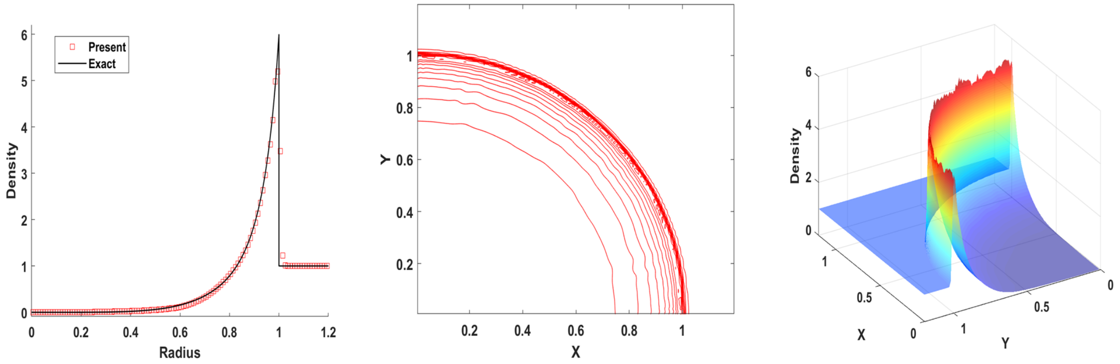

Figure 22: The numerical results for 2D Sedov Blast waves problem at time $t_{\text{final}} = 1$ with 120 mesh cells — Left: Density profile along $y = 0$ line vs the exact solution; Middle: 10 density contours from 0 to 6; Right: Surface of density profile (color and azimuth).

5.3.5. High Mach number astrophysical jets

For this case we simulate some high speed of gas flows without radiative cooling, see [HGGS05, ZS10, ZS11a]. Notice that negative density and pressure could occur for such flows.

We simulate two jets, a Mach 80 and a Mach 2000, described in [ZS10] with $\gamma = 5/3$ on a computational domain Ω. The initial condition is defined by

$$(\rho, u, v, p) = \begin{cases} (5,\ u_{\text{in}},\ 0,\ 0.4127) & \text{if } y \in [-0.05, 0.05] \\ (5,\ 0,\ 0,\ 0.4127) & \text{otherwise} \end{cases} \tag{23}$$

where $u_{\text{in}} > 0$ is the inflow jet set on a portion of the left boundary. The boundary conditions are set to outflow for the right, top and bottom boundaries. The left boundary is an inflow boundary condition.

First, we simulate a Mach 80 on $\Omega = [0, 2] \times [-0.5, 0.5]$ with $u_{\text{in}} = 30$. The numerical solutions is computed up to time $t_{\text{final}} = 0.07$ with 448×224 mesh cells. Figure 23 presents the numerical results for the density, pressure and temperature profiles in logarithmic scale. Even though very low density and pressure value occur in this test, the present scheme still performs well. The numerical results are comparable to those in [ZS10]. Moreover the present scheme captures more complex small scale structures of the flow. Second, we simulate a Mach 2000 jet on $\Omega = [0, 1] \times [-0.25, 0.25]$ by considering an inflow velocity magnitude $u_{\text{in}} = 800$. The numerical solution is computed up to time $t_{\text{final}} = 0.001$ with 640×320 mesh cells. Figure 24 presents the numerical results for density, pressure and temperature profiles in logarithmic scale. The numerical results are comparable to those in [ZS10, ZS12]. Again, the current method seems to capture more flow structures. This flow is obviously more violent than the previous one, emphasizing that the proposed numerical method is genuinely robust thanks to the MOOD loop and the first-order FV scheme used as a last resort.

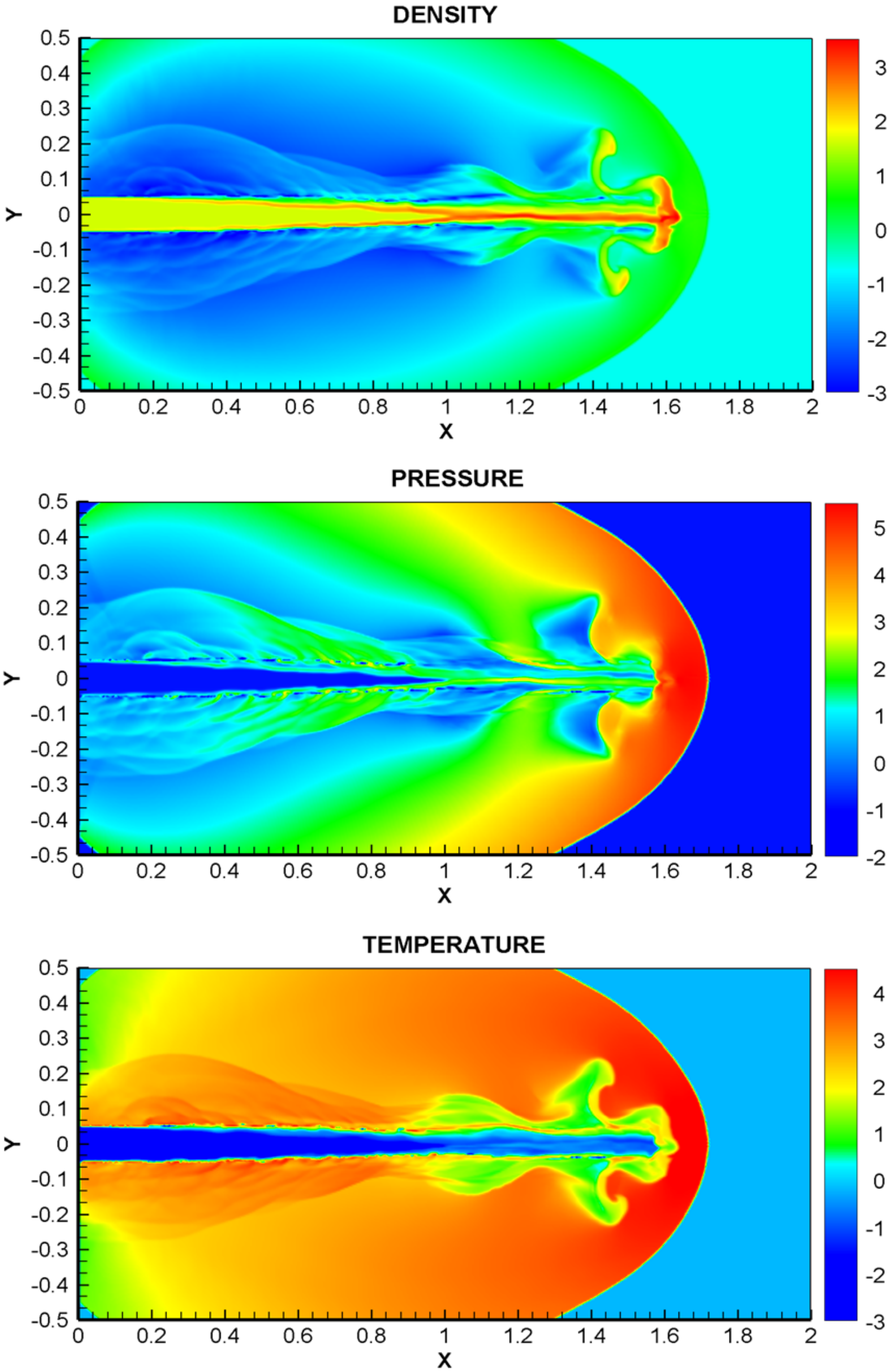

Figure 23: Numerical results for the 2D Euler equations – Mach jet 80 problem at time $t$final $= 0.07$ with 448×224 mesh cells simulated by the present scheme. Density, pressure and temperature maps in logarithmic scales.

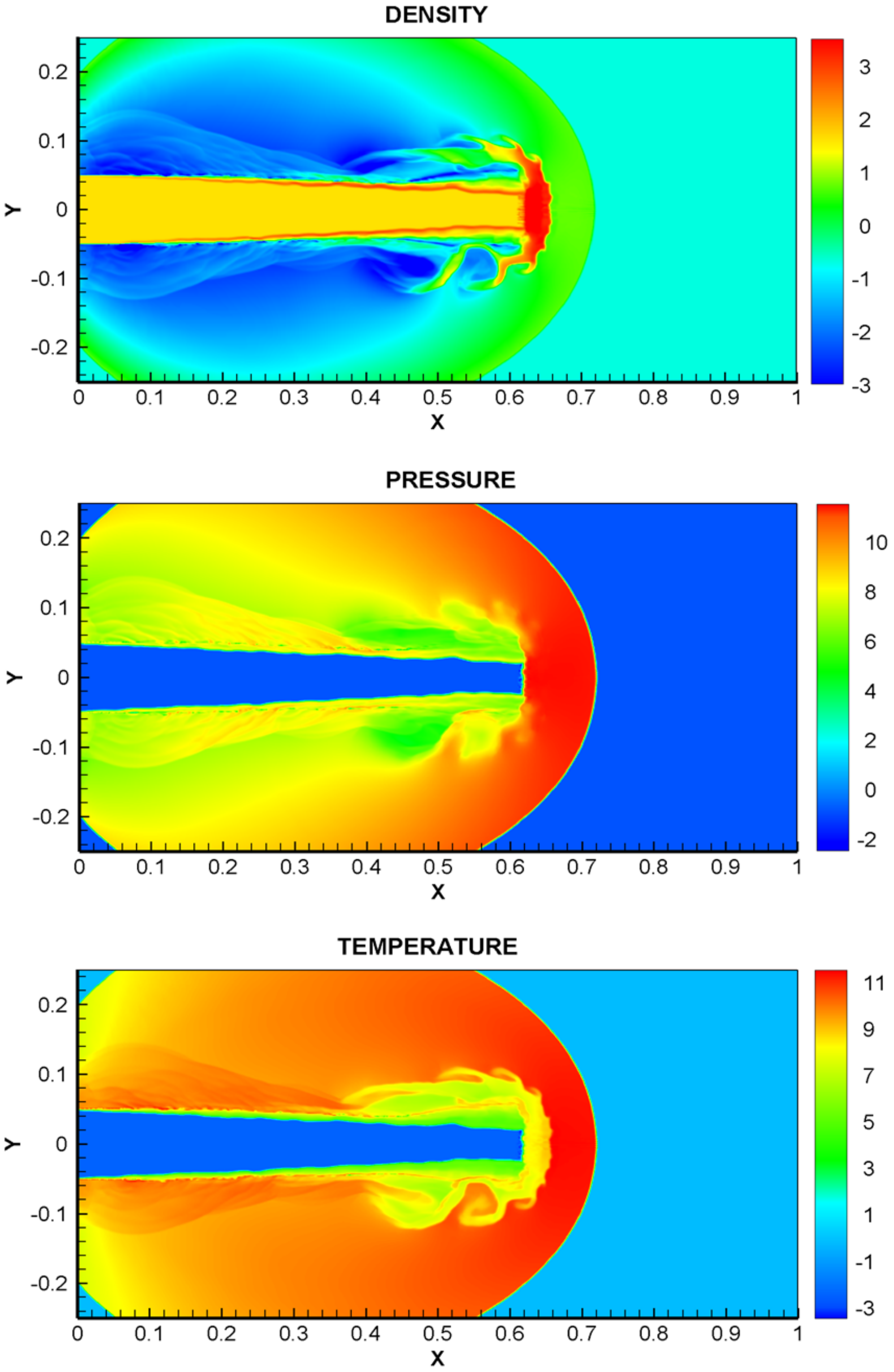

Figure 24: Numerical results for the 2D Euler equations – Mach jet 2000 problem at time $t$final $= 0.001$ with 640×320 mesh cells simulated by the present scheme. Density, pressure and temperature maps in logarithmic scales.

5.3.6. Shock Diffraction Problem

As a last test case, the shock diffraction problem has been simulated. We can find this test in the literature for the DG method [CS98, ZS10] as well as finite difference WENO schemes [ZS12]. Physically it consists of the diffraction of a shock wave at a sharp convex corner. Yet, no general theory exists which may describe this problem completely. Numerical simulations have been widely employed to understand the flow features generated by the shock diffraction, and, this problem has become popular to challenge new numerical methods. The main reason is that spurious negative density and/or pressure may be generated below and on the right of the corner. The computational domain is the union of $\Omega_1 = [0,1] \times [6,11]$ and $\Omega_2 = [1,13] \times [0,11]$. The initial condition is a pure right-moving shock of mach 5.09, initially located at $x = 0.5$ and $6 \leq y \leq 11$, and moving into the undisturbed air ahead of the shock characterized by a density of 1.4 and a pressure of 1. The boundary conditions are set to inflow at the left-most boundary $x = 0$ (for $6 \leq y \leq 11$), outflow at the right, top and bottom ones, $0 \leq y \leq 11$, $1 \leq x \leq 13$, y=0, and $0 \leq x \leq 13$, y=11, and reflective walls are considered on boundary $\Gamma_1 = \{(x,y),\ \text{s.t. } 0 \leq x \leq 1,\ y = 6\}$ and $\Gamma_2 = \{(x,y),\ \text{s.t. } 0 \leq y \leq 6,\ x = 1\}$. The specific heat ratio $\gamma = 1.4$ and final time of the computation is $t_{\text{final}} = 2.3$. In figure 25 and figure 26 we

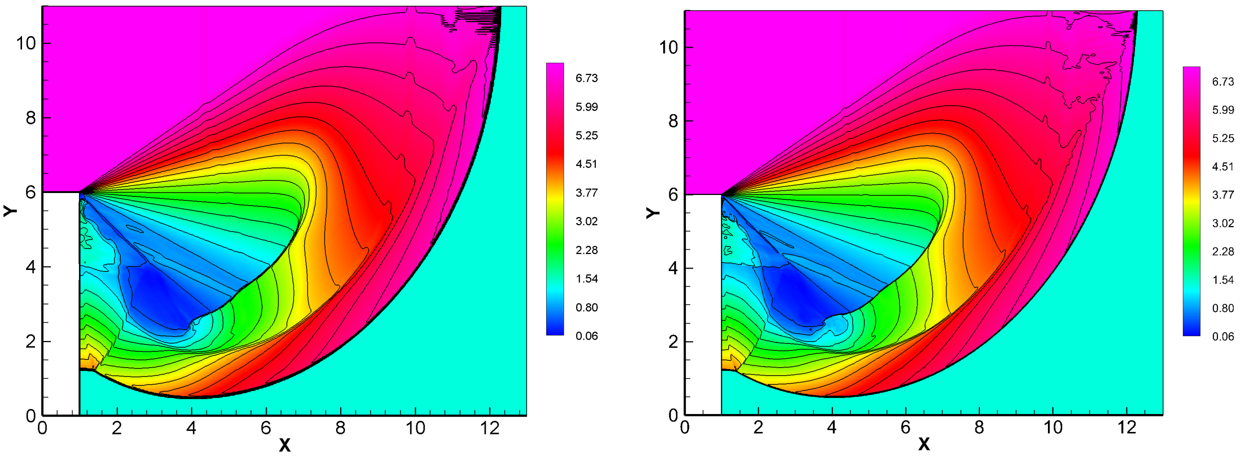

Figure 25: Numerical results for the 2D Euler equations – Shock Diffraction Problem 20 contours from 0.06 to 7.1 for density variable – Left: $\Delta x = \Delta y = \frac{1}{32}$; Right: $\Delta x = \Delta y = \frac{1}{64}$.

present respectively the density variable in color with 20 contour iso-lines spanning the interval

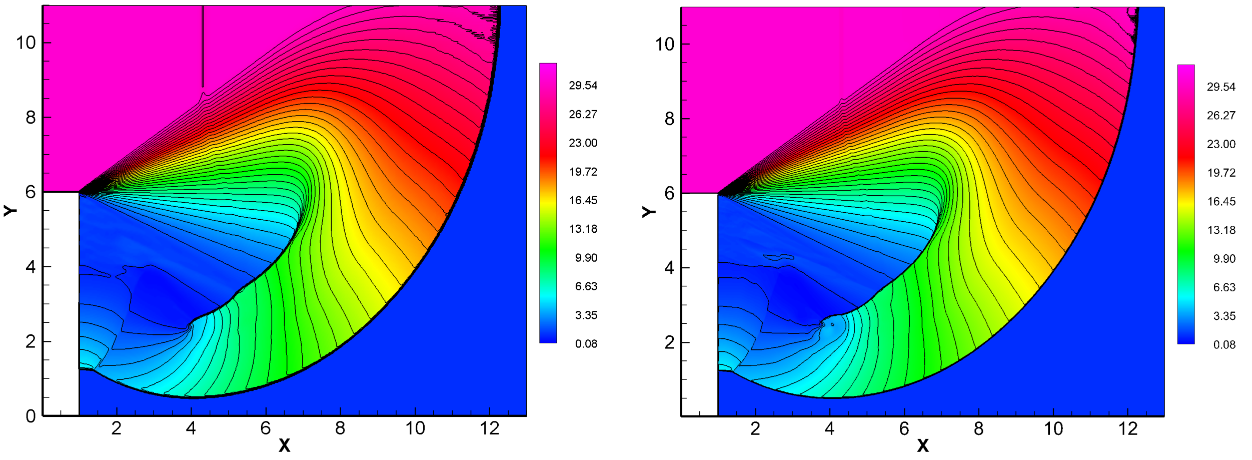

Figure 26: Numerical results for the 2D Euler equations – Shock Diffraction Problem 40 contours from 0.08 to 32 for pressure variable – Left: $\Delta x = \Delta y = \frac{1}{32}$; Right: $\Delta x = \Delta y = \frac{1}{64}$.

$[0.06, 7.1]$ and the pressure variable with 40 contour iso-lines spanning the interval $[0.08, 32]$. Two different grid resolutions are considered, $\Delta x = \Delta y = \dfrac{1}{32}$ for the left panels and $\Delta x = \Delta y = \dfrac{1}{64}$ for the right panels. We observe that the results are comparable to those in [CS98, ZS10, ZS12] for the main flow structures. In our simulations, the MOOD loop allows to handle appropriately the occurrence of negative density or pressure which are cured by the use of the first-order FV scheme when needed. This allows the present scheme to become "fail-safe" to non-admissible physical Moreover the finer grid resolution allows to observe sharper discontinuities without the creation of spurious oscillations.

5.3.7. Diagnostics on reconstruction selection for 2D Euler equations

Likewise for the 1D tests, in table 5 we present the percentage of cells for the four characteristic variables W_1, W_2, W_3, W_4 which are dealt with the HO, SHARP, ENO and piece-wise constant (P0) reconstructions. The tests are the 2D Sedov Blast waves, Mach 80 jet, Mach 2000 jet, shock-vortex interaction and shock diffraction problem with $\Delta x = \Delta y = \frac{1}{32}$. One sums up for every 10 time steps and final time step the number of cells using the same reconstruction and further takes the percentage with respect to the total number: $\frac{N_t}{10} \times (N_x \times N_y) + N_x \times N_y$. Each test case produces different flow patterns and the scheme does adapt. Consequently, for the reconstructions, we can not identify a general behavior which was expected. However, it seems that the HO reconstruction (target 5th order accuracy without dissipation) is selected for about 30% up to 83% of cells. The dissipative ENO reconstructions are selected between 9% to 28% of cells while the sharp reconstruction is chosen for 6% up to 58% of cells. At last the piece-wise constant reconstruction is almost never selected (maximal 0.05%). But, recall that each time it is selected then it means that the code has created a non-physical state. In other words the code has been simply saved from code-crashing[2].

---

[2] Note that 0.05% of the cells for the Mach 80 jet problem may seem rather small. However it corresponds to about 81000 cells among the 162 millions of cell updates computed during the whole simulation.

Test	$N_t, N_x \times N_y$	W_1/W_3				W_2/W_4			
		SH	HO	ENO	P0	SH	HO	ENO	P0
Shock-V	657, 200x200	6.56%	65.32%	28.12%	0%	58.72%	31.63%	9.64%	0%
		10.38%	65.49%	25.06%	0%	7.94%	64.24%	27.82%	0%
Sedov	3441, 120x120	7.22%	81.41%	11.37%	0%	6.51%	81.1%	12.39%	0%
		5.99%	81.79%	12.22%	0%	9.75%	80.57%	9.68%	0%
M-80	1613, 448x224	9.25%	77.9%	12.8%	0.05%	9.85%	76.49%	13.61%	0.05%
		9.64%	78.09%	12.22%	0.05%	9.77%	77.28%	12.9%	0.05%
M-2000	1904, 640x320	6.95%	83.20%	9.81%	0.04%	7.58%	82.25%	10.13%	0.04%
		7.27%	83.33%	9.36%	0.04%	8.00%	82.44%	9.51%	0.04%
Shock-D	1708, 416x352	8.28%	77.74%	13.98%	1E-4%	7.97%	78.14%	13.89%	1E-4%
		17.06%	71.89%	11.05%	1E-4%	10.43%	76.8%	12.77%	1E-4%

Table 5: Percentage of cells dealt with the $\mathrm{SHARP}, \mathrm{HO}, \mathrm{ENO}, \mathrm{P0}$ reconstructions for the four characteristic variables W_1, W_2, W_3, W_4 and five test cases.

6. Conclusions and perspectives

In this paper we have presented a reconstruction strategy to be employed in Finite Volume (FV) scheme which differs from classical polynomial-based with *a priori* limiting strategy. Most of classical schemes are based on a (linear) polynomial reconstruction, which is further supplemented with a non-linear limiter: classical slope limiter for piece-wise linear reconstruction, (C)WENO blending, hierarchical moment limiter, artificial viscosity, etc. As such the accuracy in space of such FV schemes, measured for smooth solutions, is obtained by the accuracy with which the polynomials are reconstructed. In other words the polynomial degree drives the scheme accuracy. Meanwhile, the robustness and non-oscillatory behavior are obtained by the non-linear limiter which is often computed just after the reconstructions.

Our approach differs because our cell-based reconstruction procedure relies on several types of reconstructions: (1) 5th order accurate polynomials for smooth solutions, (2) viscous non-linear THINC functions to add dissipation and (3) sharp non-linear ones to handle discontinuity and steep gradients, and, at last, (4) no reconstruction at all for extreme situations.

The fundamental mechanism in our approach to choose between these reconstructions relies on the BVD (Bounded Variation Diminishing) strategy. The reconstruction in one cell is chosen to be the one producing the smallest jumps at the cell interfaces. With BVD the reconstruction is polynomial $\mathbb{P}_4$ for smooth solutions, viscous on non-smooth solution (like a limited $\mathbb{P}_1$ reconstruction) and adopts a step-like shape for genuine discontinuous solution. Moreover, an *a posteriori* loop is added to the scheme to ensure that in the case the obtained numerical solution at time t^{n+1} does not ensure fundamental properties like the positivity, computer representation, then, locally, the solution is recomputed with a first-order accurate FV scheme, *i.e.* without any reconstruction. As such a solution property preserving non-linear reconstruction procedure for Finite Volume scheme is designed. The rest of the FV scheme employs a HLLC flux, a Runge-Kutta time discretisation and dimension splitting to avoid costly multidimensional polynomial reconstructions. The goal is not to develop a provable optimal high accurate numerical method for smooth flows. Rather, the purpose of this work is to provide an efficient replacement for the pair (polynomial reconstruction, limiter) used in classical FV scheme (TVD, WENO, etc.). Indeed in our approach the scheme must select among several reconstructions, the most appropriate one according to goodness criteria. Some criteria are set *a priori* with BVD, some are verified *a posteriori* with MOOD. Being fundamentally 1D, the FV scheme proposed in this work is genuinely inexpensive. The numerical results prove that the scheme can capture both contact discontinuities and shocks on only two cells in 1D. Remarkably, such sharp interfaces can not generally be obtained with the state of the art FV schemes of high accuracy. This behavior is confirmed on 2D test problems for which the numerical method present genuinely sharp discontinuity for a second-order accurate scheme according to classical numerical analysis. The scheme is extremely robust to positivity issues due to the *a posteriori* treatment and, at last, the directional splitting yields a very reasonable cost for such apparent accuracy. In the future, we plan to extend the approach to unstructured meshes and three dimensions. Moreover, the application of this scheme to more complex PDEs with stiff source terms (chemical reactions, multiphase flows, etc.) is a clear nearby perspective because the accuracy in capturing sharp fronts is of paramount importance for such models.

Acknowledgments

Parts of this work has been managed while R.L. was invited to visit Xiao's Lab at the Tokyo Institute of Technology, R.L. acknowledges the financial support for this visit by Pr. F. Xiao. This work was supported in part by the fund from JSPS (Japan Society for the Promotion of Science) under Grant Nos. 17K18838 and 18H01366.

References

[ABC16] F. Acker, R. Borges, and B. Costa. An improved weno-z scheme. *J. Comput. Phys.*, 313:726–753, 2016.

[Bal10] D.S. Balsara. Multidimensional HLLE Riemann solver: Application to Euler and magnetohydrodynamic flows. *Journal of Computational Physics*, 229:1970–1993, 2010.

[Bal12] D.S. Balsara. A two-dimensional HLLC Riemann solver for conservation laws: Application to Euler and magnetohydrodynamic flows. *Journal of Computational Physics*, 231:7476–7503, 2012.

[BDA14] D.S. Balsara, M. Dumbser, and R. Abgrall. Multidimensional HLLC Riemann Solver for Unstructured Meshes - With Application to Euler and MHD Flows. *Journal of Computational Physics*, 261:172–208, 2014.

[BDLM18] W. Boscheri, M. Dumbser, R. Loubère, and P.H. Maire. A second-order cell-centered lagrangian ader-mood finite volume scheme on multidimensional unstructured meshes for hydrodynamics. *Journal of Computational Physics*, 358:103 – 129, 2018.

[BLD15] W. Boscheri, R. Loubère, and M. Dumbser. Direct arbitrary-lagrangian–eulerian ader-mood finite volume schemes for multidimensional hyperbolic conservation laws. *Journal of Computational Physics*, 292:56 – 87, 2015.

[BT17] F. Blachère and R. Turpault. An admissibility and asymptotic preserving scheme for systems of conservation laws with source term on 2d unstructured meshes with high-order mood reconstruction. *Computer Methods in Applied Mechanics and Engineering*, 317:836 – 867, 2017.

[CDL11] S. Clain, S. Diot, and R. Loubère. A high-order finite volume method for systems of conservation laws—multi-dimensional optimal order detection (mood). *J. Comput. Phys.*, 230:4028–4050, 2011.

[CF17] S. Clain and J. Figueiredo. The mood method for the non-conservative shallow-water system. *Computers & Fluids*, 145:99 – 128, 2017.

[CS98] B. Cockburn and C.W. Shu. The runge–kutta discontinuous galerkin method for conservation laws v: Multidimensional systems. *Journal of Computational Physics*, 141(2):199 – 224, 1998.

[CW84] P. Colella and P. Woodward. The piecewise parabolic method (ppm) for gas-dynamical simulations. *J. Comput. Phys.*, 54(1):174 – 201, 1984.

[DCL12] S. Diot, S. Clain, and R. Loubère. Improved detection criteria for the multi-dimensional optimal order detection (mood) on unstructured meshes with very high-order polynomials. *Computers & Fluids*, 64:43–63, 2012.

[DIX$^+$18] X. Deng, S. Inaba, B. Xie, K.M. Shyue, and F. Xiao. High fidelity discontinuity-resolving reconstruction for compressible multiphase flows with moving interfaces. *Journal of Computational Physics*, 371:945 – 966, 2018.

[DL16] M. Dumbser and R. Loubère. A simple robust and accurate a posteriori sub-cell finite volume limiter for the discontinuous galerkin method on unstructured meshes. *Journal of Computational Physics*, 319:163 – 199, 2016.

[DSX18] X. Deng, Y. Shimizu, and F. Xiao. Constructing high-order discontinuity-capturing schemes with linear-weight polynomials and boundary variation diminishing algorithm. *arXiv preprint*, arXiv:1811.08316, 2018.

[DSX19] X. Deng, Y. Shimizu, and F. Xiao. A fifth-order shock capturing scheme with two-stage boundary variation diminishing algorithm. *Journal of Computational Physics*, 386:323–349, 2019.

[DXL$^+$18] X. Deng, B. Xie, R. Loubère, Y. Shimizu, and F. Xiao. Limiter-free discontinuity-capturing scheme for compressible gas dynamics with reactive fronts. *Computers & Fluids*, 171:1–14, 2018.

[DZLD14] M. Dumbser, O. Zanotti, R. Loubère, and S. Diot. A posteriori subcell limiting of the discontinuous galerkin finite element method for hyperbolic conservation laws. *J. Comput. Phys.*, 278:47–75, 2014.

[FHA16] L. Fu, X.Y. Hu, and N.A. Adams. A family of high-order targeted eno schemes for compressible-fluid simulations. *Journal of Computational Physics*, 305:333 – 359, 2016.

[God59] S.K. Godunov. A difference method for numerical calculation of discontinuous solutions of the equations of hydrodynamics. *Matematicheskii Sbornik*, 89:271–306, 1959.

[Got05] S. Gottlieb. On high order strong stability preserving runge-kutta and multi step time discretizations. *J. Sci. Comput.*, 25:105–128, 2005.

[HGGS05] Y. Ha, C. Gardner, A. Gelb, and C.W. Shu. Numerical simulation of high mach number astrophysical jets with radiative cooling. *Journal of Scientific Computing*, 24(1):29–44, Jul 2005.

[Huy97] H.T. Huynh. Schemes and constraints for advection time stepping method with flux reconstruction view project. *Art. Lec. Notes Phys.*, 1997.

[JS96] G.S. Jiang and C.W. Shu. Efficient implementation of weighted eno schemes. *J. Comput. Phys.*, 126:202–228, 1996.

[JYY18] Z.H. Jiang, C. Yan, and J. Yu. Efficient methods with higher order interpolation and mood strategy for compressible turbulence simulations. *Journal of Computational Physics*, 371:528 – 550, 2018.

[KT02] A. Kurganov and E. Tadmor. Solution of two-dimensional Riemann problems for gas dynamics without Riemann problem solvers. *Numer. Methods Partial Differential Equations*, 18:584–608, 2002.

[LCS09] W. Liu, J. Cheng, and C.W. Shu. High order conservative lagrangian schemes with lax-wendroff type time discretization for the compressible euler equations. *J. Comput. Phys.*, 228(23):8872–8891, December 2009.

[LDD14] R. Loubère, M. Dumbser, and S. Diot. A new family of high order unstructured mood and ader finite volume schemes for multidimensional systems of hyperbolic conservation laws. *Communications in Computational Physics*, 16(3):718–763, 2014.

[Lee79] B. Van Leer. Towards the ultimate conservative difference scheme. v. a second-order sequel to godunov's method. *Journal of Computational Physics*, 32(1):101 – 136, 1979.

[LK16] C. Lohmann and D. Kuzmin. Synchronized flux limiting for gas dynamics variables. *Journal of Computational Physics*, 326:973 – 990, 2016.

[LLZ15] Q. Li, P. Liu, and H. Zhang. Piecewise polynomial mapping method and corresponding weno scheme with improved resolution. *Commun. Computat. Phys.*, 18(5):1417–1444, 2015.

[LR97] T. Linde and P.L. Roe. Robust euler codes. *in: Thirteenth Computational Fluid Dynamics Conference*, pages AIAA–97–2098, 1997.

[LS05] R. Loubère and M.J. Shashkov. A subcell remapping method on staggered polygonal grids for arbitrary-lagrangian–eulerian methods. *Journal of Computational Physics*, 209(1):105 – 138, 2005.

[LW03] R. Liska and B. Wendroff. Comparison of several difference schemes on 1d and 2d test problems for the euler equations. *SIAM J. Scientific Computing*, 25(3):995–1017, 2003.

[Pir06] S. Pirozzoli. On the spectral properties of shock-capturing schemes. *Journal of Computational Physics*, 219(2):489 – 497, 2006.

[RCD03] A. Rault, G. Chiavassa, and R. Donat. Shock-vortex interactions at high mach numbers. *Journal of Scientific Computing*, 19:347–371, 2003.

[RLZ03] Y.X. Ren, M. Liu, and H. Zhang. Efficient implementation of weighted eno schemes. *J. Comput. Phys.*, 192:365–386, 2003.

[RSS13] J. Reisner, J. Serencsa, and S. Shkoller. A space–time smooth artificial viscosity method for nonlinear conservation laws. *Journal of Computational Physics*, 235:912 – 933, 2013.

[Ruu] Steven J. Ruuth. Global optimization of explicit strong-stability-preserving runge-kutta methods.

[Sed59] L.I. Sedov. *Similarity and Dimensional Methods in Mechanics.* Academic Press, New York, 1959.

[SIX16] Z. Sun, S. Inaba, and F. Xiao. Boundary variation diminishing (bvd) reconstruction: A new approach to improve godunov schemes. *J. Comput. Phys.*, 322:309–325, 2016.

[SO88] C.W. Shu and S. Osher. Efficient implementation of essentially non-oscillatory shock-capturing schemes. *J. Comput. Phys.*, 77:439–471, 1988.

[SO89] C.W. Shu and S. Osher. Efficient implementation of essentially non-oscillatory shock-capturing schemes, ii. *J. Comput. Phys.*, 83:32–78, 1989.

[SR93] C.W. Schulz-Rinne. Classification of the Riemann problem for two-dimensional gas dynamics. *SIAM J. Math. Anal.*, 24:76–88, 1993.

[SR02] R. J. Spiteri and S. J. Ruuth. A new class of optimal high-order strong-stability-preserving time discretization methods. *SIAM J. Numer. Anal.*, 40(2):469–491, February 2002.

[SX14] K.M. Shyue and F. Xiao. An eulerian interface sharpening algorithm for compressible two-phase flow: The algebraic thinc approach. *J. Comput. Phys.*, 268:326–354, 2014.

[TB19] R. Turpault and T.H. Nguyen Bui. A high order mood method for compressible navier-stokes equations: application to hypersonic viscous flows. *Progress in Computational Fluid Dynamics,*, 2019. in press.

[Tor09] E.F. Toro. *Riemann solvers and numerical methods for fluid dynamics: a practical introduction*. Springer Verlag, 2009.

[Vil18] F. Vilar. A posteriori correction of high-order discontinuous galerkin scheme through subcell finite volume formulation and flux reconstruction. *Journal of Computational Physics*, 2018.

[WA08] L. White and A. Adcroft. A high-order finite volume remapping scheme for nonuniform grids: The piecewise quartic method (pqm). *J. Computat. Phys.*, 227(15):7394–7422, 2008.

[WC84] P. Woodward and P. Colella. The numerical simulation of two-dimensional fluid flow with strong shocks. *Journal of Computational Physics*, 54:115–173, 1984.

[XHK05] F. Xiao, K. Honma, and T. Kono. A simple algebraic interface capturing scheme using hyperbolic tangent function. *int. J. Methods Fluids*, 48:1023–1040, 2005.

[XIC11] F. Xiao, S. Ii, and C. Chen. Revisit to the thinc scheme: A simple algebraic vof algorithm. *J. Comput. Phys.*, 230:7086–7092, 2011.

[XZ17] Z. Xu and X. Zhang. Chapter 4 - bound-preserving high-order schemes. In R. Abgrall and C.W. Shu, editors, *Handbook of Numerical Methods for Hyperbolic Problems*, volume 18 of *Handbook of Numerical Analysis*, pages 81 – 102. Elsevier, 2017.

[ZS10] X. Zhang and C.W. Shu. On positivity-preserving high order discontinuous galerkin schemes for compressible euler equations on rectangular meshes. *J. Comput. Phys.*, 229:8918–8934, 2010.

[ZS11a] X. Zhang and C.W. Shu. Maximum-principle-satisfying and positivity-preserving high-order schemes for conservation laws: survey and new developments. *Proceedings of the Royal Society A: Mathematical, Physical and Engineering Sciences*, 467(2134):2752–2776, 2011.

[ZS11b] X. Zhang and C.W. Shu. Positivity-preserving high order discontinuous galerkin schemes for compressible euler equations with source terms. *J. Comput. Phys.*, 230(4):1238–1248, 2011.

[ZS12] X. Zhang and C.W. Shu. Positivity-preserving high order finite difference weno schemes for compressible euler equations. *J. Comput. Phys.*, 231:2245–2258, 2012.